Design and Fabrication of Electron Energy Filters for Room Temperature Inelastic Electron Tunneling Spectroscopy

by

Prashant Patil

Submitted to the Program in Media Arts and Sciences,
School of Architecture and Planning
in partial fulfillment of the requirements for the degree of

Master of Science

at the

MASSACHUSETTS INSTITUTE OF TECHNOLOGY

September 2013

Signature redacted

Author .....
Program in Media Arts and Sciences
August 9, 2013

Signature redacted

Certified by ... .
Prof. Neil Gershenfeld
Director, MIT Center for Bits and Atoms
Thesis Supervisor

Signature redacted

Accepted by..... .....
Prof. Patricia Maes
Associate Academic Head
Program in Media Arts and Sciences

Design and Fabrication of Electron Energy Filters for Room Temperature Inelastic Electron Tunneling Spectroscopy

by

Prashant Patil

Submitted to the Program in Media Arts and Sciences
on August 9, 2013, in partial fulfillment of the
requirements for the degree of
Master of Science

Abstract

Odor detection has wide range of applications in a variety of industries, including the agricultural, clinical diagnosis, pharmaceutical, cosmetics, food analysis, environmental and defense fields. Spectroscopic techniques such as FTIR and Raman are commonly used for electronic nose application. However, their application is limited by factors such as poor sensitivity, selectivity and non-portability.

Inelastic electron tunneling spectroscopy (IETS) is an all electronic spectroscopy that has been extensively used to measure the vibrational modes of molecules and can be used for electronic nose application. It has several advantages such as ultra-high sensitivity and compact size. However, IETS requires cryogenic temperature to resolve molecular spectra, which limits its use in electronic nose application. A new theory of biological olfaction postulates that the odorant detectors inside a nose recognize an odorant's vibrations via inelastic electron tunneling (Turin, 1996). However, a biological system works at room temperature but conventional IET spectroscopy requires cryogenic temperatures. Thus posing the following question: Is it possible to resolve molecular vibrational spectra using inelastic electron tunneling spectroscopy at room temperature?

IET spectroscopy involves the tunneling of electrons through an insulating barrier that is situated between two conducting metal electrodes. At room temperature, tunneling electrons possess thermal energy and occupy broad distribution of energy levels available in metals. This thermal distribution of electrons drastically reduces the resolution of IET spectroscopy. By reducing the thermal distribution of tunneling electrons at room temperature, we can increase the resolution of IET spectroscopy.

The objective of this work is to develop electron energy filters to narrow down the thermal energy distribution of electrons at room temperature. I further evaluate the application of these electron energy filters to increase the resolution of IET spectroscopy at room temperature. Some recent advancements in nanomaterials, such as quantum dots with discrete electron energy levels are an excellent choice as electron energy filters. In metals, the continuous distribution of available energy states causes broad thermal distribution of electrons at room temperature. In contrast, quantum dots have discrete energy levels due to their small size. So even though electrons might possess thermal energy at room temper-

ature, they can only occupy the discrete energy levels available in quantum dots. Hence, the thermal energy distribution of electrons can be narrowed down to the energy levels available in quantum dots.

The electron energy filter designed in this work, consists of a 2-dimensional array of CdSe quantum dots of sizes around 2.5nm sandwiched between metal electrodes. Through electrical characterization of these devices, we can conclude that they can narrow down thermal distribution of electrons from 25meV down to around 10meV. However, to resolve the molecular vibrational energy level at room temperature, thermal energy distribution of electrons should be less than 6.6meV. Since array of quantum dots results in formation of energy minibands, this work suggests that single quantum dot should be used instead of array of dots to improve the performance of electron energy filters. Moreover, the study of electron transport through single quantum dots done in this work suggests that the size of the dot should be less than 2.5nm to be used in room temperature IET spectroscopy.

Interestingly, this length scale is consistent with the size of donor and acceptor sites in odorant receptors potentially explaining how these receptors could be able to resolve molecular spectra at room temperatures.

Thesis Supervisor: Prof. Neil Gershenfeld
Title: Director, MIT Center for Bits and Atoms

Design and Fabrication of Electron Energy Filters for Room Temperature Inelastic Electron Tunneling Spectroscopy

by

Prashant Patil

The following people served as readers for this thesis:

Signature redacted

Thesis Reader .....

Joseph M. Jacobson
Associate Professor of Media Arts and Sciences
Program in Media Arts and Sciences

Signature redacted

Thesis Reader .....

Andreas Mershin
Research Scientist
MIT Center for Bits and Atoms

Acknowledgments

I thank Neil Gershenfeld, my thesis advisor, for his guidance, for teaching me how to do research. For buying me cool toys and letting me play with exciting one. Your guidance has been invaluable in bringing this work to fruition.

I thank Joe Jacobson, every conversation I have had with you has been enlightening, empowering, refreshing, provocative, and always instructive.

I thank Andreas Mershin, a long a steadfast critic and ultimately a guiding hand. You have added additional focus on questions relating to this work.

I thank Luca, for getting me thinking about the problems in this thesis. Without you, this thesis would have been about some other topic entirely.

I thank Nadya, you have been instrumental in my journey from IIT to MIT. When I first met you in a workshop in Pune, I would have never thought that I would someday be working with you.

I thank John D and Tom, for shop training's and keeping us safe.

I thank Joe Murphy, you have always manage to sort out things for us. Thanks for considering our carelessness as your own last minute emergency

I thank Ryan, for ordering long list of items and always helping skinny grad student

I thank Theresa, for taking time to chat with us and reminding us life beyond lab. Feeding us with delicious food.

I thank Kenny, you have always been available for valuable suggestion on making things

I would like to thank Kurt Broderick mMrk Mondol for assisting me in learning the various processes and systems in the microelectronics technology laboratory (MTL).

In addition a thank you to Professor K. W. Hipps of Washington State University for valuable suggestions on fabrication of IETS devices.

Special gratitude must go to Charles Fracchia, Noah Jakimo, Thomas Duval, Sam Calisch, Will Langford, James Pelletier, Lisa and Divya for there direct and indirect help in this work. – thank you all.

Contents

List of Figures

List of Tables

Chapter 1

Introduction

The major applications of odor detection are in the agricultural industry, clinical diagnosis, pharmaceutical, cosmetics, food analysis, environmental and defense. In food industry, it is used to check quality of ingredients and spoilage, to monitor livestock and poultry facilities. In biomedical industry it is used for diagnosis of variety of diseases by breath analysis. Molecular vibrational spectroscopy is commonly used for odorant recognition. The vibrations of the chemical bonds in a molecule occur at specific frequencies. This vibrational spectrum is unique for every molecule and acts as a molecular fingerprint. Thus vibrational spectrum of a molecule be used for molecular identification and characterization. Optical spectroscopic techniques such as FTIR and Raman are commonly used to measure vibrational spectrum of molecules. But these techniques require complex optics, are bulky and consume high power. This limits there usability in electronic nose application.

Inelastic electron tunneling spectroscopy (IETS) is a type of vibrational spectroscopy that extracts the vibrational spectra of molecules adsorbed into the insulator layer of a tunnel junction. As opposed to other vibrational spectroscopy, IETS does not require complex optics and has low power consumption. It is also an all electronic spectroscopy so even optically forbidden transitions which are invisible in FTIR and Raman can also be observed in inelastic electron tunneling spectroscopy. Because of its ultra-high sensitivity, low power consumption and portability, IETS is an

excellent candidate for electronic nose application.

1.1 Inelastic Electron Tunneling Spectroscopy

The phenomenon of Inelastic electron tunneling was first observed by Jaklevic and Lamb[2] in 1966 . It was observed that the conductance of a metal-insulator-metal junction increases at a certain characteristics bias voltages. These voltages correspond to the vibrational energy levels of the impurity molecules adsorbed in the insulating tunneling junction. It was found that tunneling electrons were actually interacting with the vibrational states of impurity molecules.

Since then Inelastic electron tunneling spectroscopy (IETS) is successfully applied to study molecular vibrational and electronic spectroscopy. An IETS device consists of a metal-insulator-adsorbent-metal structure as shown in figure 1.1 . The molecules under study are introduced into

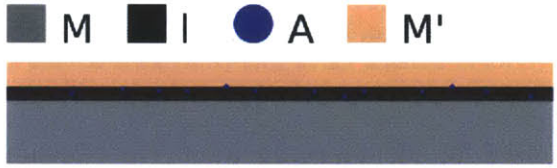

Figure 1.1: conventional metal-insulator-metal IETS Devices

the tunneling junction during the fabrication of device. By measuring the current-voltage characteristics of these metal-insulator-adsorbent-metal devices in a special way, vibrational modes of adsorbed molecules can be determined.

Vibrational energy levels observed in inelastic electron tunneling spectroscopy coincide with the vibrational energy levels observed in other spectroscopy techniques such as fast Fourier transform spectroscopy (FTIR) and Raman spectroscopy. Figure 1.2 shows the vibrational energy levels of cesium salt of pentacyanopropenide, *CsPCP* observed using IETS , FTIR and Raman. Inelastic electron tunneling spectroscopy has several advantages over other spectroscopy techniques such as FTIR and Raman spectroscopy. These advantages are as follows -

1. Ultra-high sensitivity: Only less than 10^{13} molecules are required to provide an IETS spectra[3].

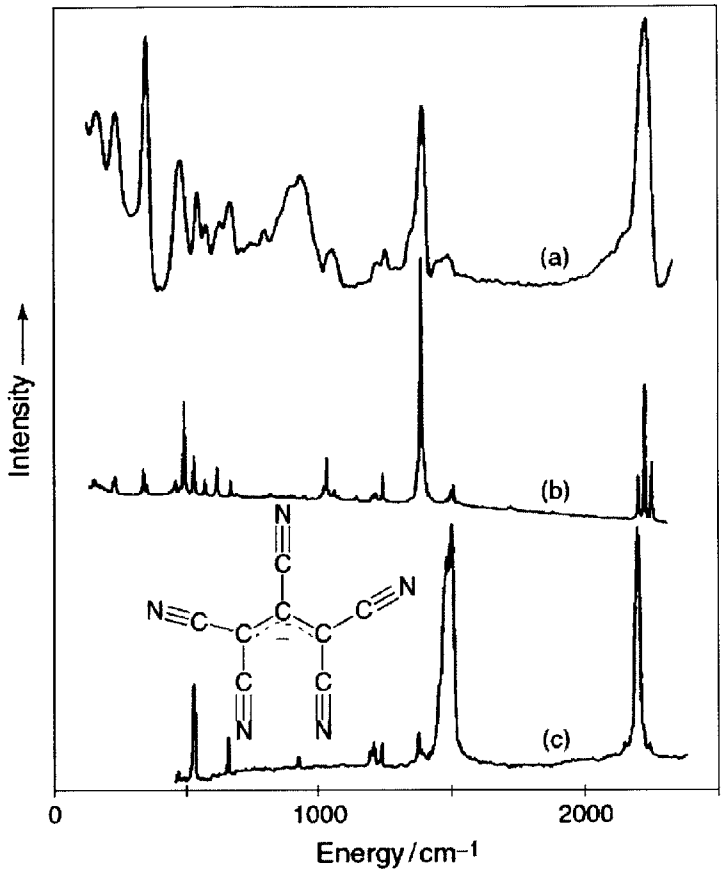

Figure 1.2: Comparison of vibrational energy peaks observed in IETS, FTIR and Raman spectroscopy [4]

2. Even optically forbidden transitions which are invisible in FTIR and Raman spectroscopy[5] can also be observed in inelastic electron tunneling spectroscopy.

1.2 Theory of Inelastic Electron Tunneling Spectroscopy

The phenomenon of inelastic electron tunneling spectroscopy can be easily understood by considering the band-diagram of metal-insulator-adsorbent-metal devices shown in figure 1.3. When a bias voltage is applied across the junction, electrons tunnel through tunneling barrier and contribute to current. This mode of tunneling is known as elastic tunneling as the energy of the electrons are conserved during tunneling. As the bias voltage is gradually increased, at a characteristic volt-

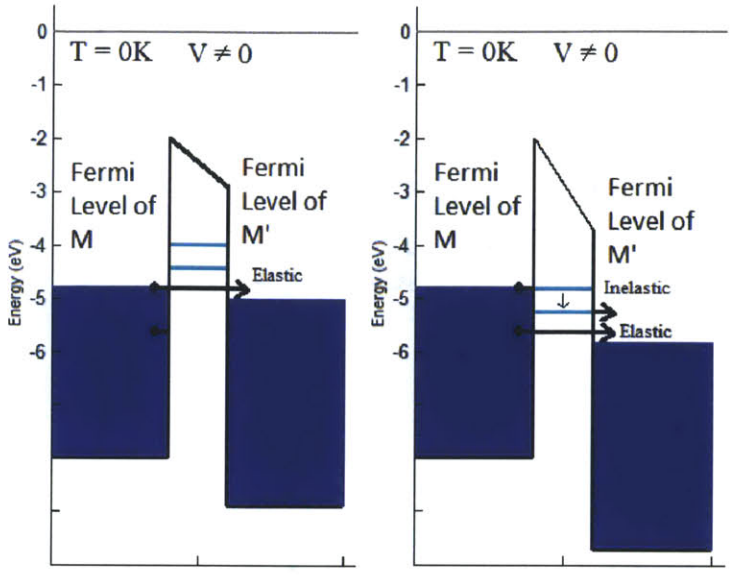

Figure 1.3: Band diagram of metal-insulator-metal device

age, electrons now have sufficient energy to excite the vibrational energy level of the adsorbed molecules. These electrons during tunneling can loose part of their energy to excite the vibrational energy level of adsorbed molecules. This mode of tunneling is know as inelastic tunneling as energy of the electrons are not conserved. This process is schematically shown in figure 1.3(b).

Once the applied bias voltage exceeds this characteristics voltage, the total tunneling current now consist of both elastic tunneling current and inelastic tunneling current. This addition of extra channel of inelastic tunneling current results in an increase in the conductance of these devices. Figure 1.4 schematically shows the current-voltage characteristics of a metal-insulator-adsorbate-metal device. For a bias voltage $V < \frac{hv}{e}$, the current only constitutes of elastic tunneling current. When bias voltage exceeds $\frac{hv}{e}$ which is the vibrational energy level of the adsorbed molecule, the current constitute of both elastic and inelastic tunneling current. This increase in conductance results in change in slop of current-voltage curve. Since inelastic current constitutes only 1% of the total current, this change in slop is not visible in a practical current voltage characteristics.

This small change in conductance i.e. change in slop of IV curve appears as step in dI/dV *vs* V plot and as a peak in d^2I/dV^2 *vs* V plot as shown in figure 1.5(a) . Since peak position can easily be identified as compare to change in slop in IV curve or steps in dI/dV *vs* V , the plot between

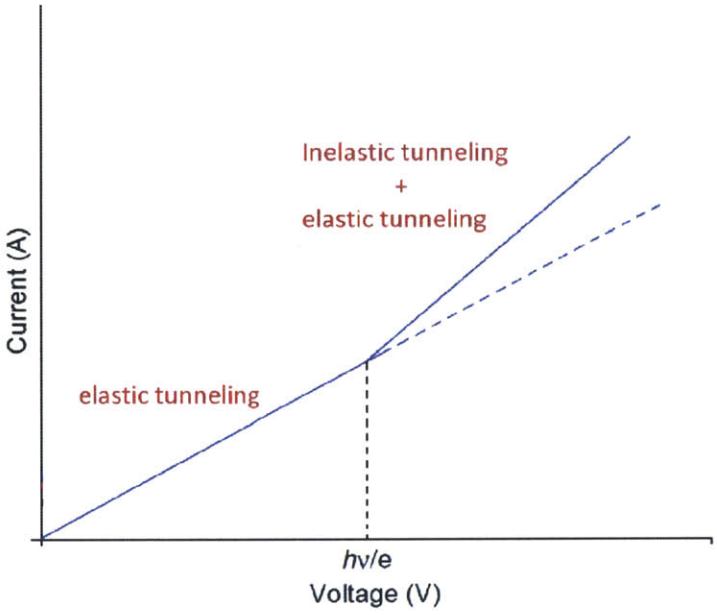

Figure 1.4: Schematic representation of Current-Voltage characteristics of metal-insulator-metal tunneling junction

d^2I/dV^2 *vs* V is commonly used for inelastic electron tunneling spectroscopy. The plot between d^2I/dV^2 *vs* V is known as inelastic electron tunneling spectra and the observed peaks are known as IETS peaks.

The resolution of inelastic electron tunneling spectroscopy depends upon how sharply the extra channel of inelastic tunneling current is added to the total current. If this addition of inelastic tunneling current is a gradual process as compare to an abrupt process as shown in figure 1.5(b), the observed IETS peaks are very broad. The resolution of inelastic electron tunneling spectroscopy is determined by the FWHM (full width at half maximum) of IETS peaks. In order to resolve the vibrational energy levels of molecules, the resolution of inelastic tunneling spectroscopy should be less than $\sim 50mV$. Typically, electrons at room temperature have energy of the order of $\sim 25mV$. Thus, at room temperature due to this thermal energy of electrons, the observed IETS peaks are broad, which limits the resolution for measurement of vibrational energy level of molecules. In order to avoid this thermalization of electrons, IETS is usually performed at cryogenic temperature ($4.2K$). This requirement of cryogenic temperature for IETS measurements, limits the application

of IETS for sensing application such as gas sensors and electronic nose.

1.3 Electron Energy Filters for Room Temperature IETS

The resolution of IET spectroscopy is temperature dependent. In order to resolve molecular vibrations using IETS, experiment should be performed at cryogenic temperature. At room temperature, tunneling electrons possess thermal energy and occupy broad distribution of energy levels available in metals. This thermal distribution of electrons results in thermal broadening on IETS peak which drastically reduced the resolution of IETS spectroscopy.

A new theory of biological olfaction postulates that the odorant detectors inside nose recognizes an odorant's vibrations via inelastic electron tunneling[1]. A biological system must work at ambient or body temperature, i.e. at $300K$. When IETS is performed between metal electrodes, the tunneling junction is cooled to cryogenic temperatures to increase resolution to resolve vibrational energy level of molecules. This pose a question " Is it possible to resolve molecular vibrational spectra using inelastic electron tunneling spectroscopy at room temperature?"

In order to perform inelastic electron tunneling spectroscopy at room temperature with a resolution to measure vibrational energy levels of molecules, we have to minimize the thermalization of electrons at room temperature. In metals, continuous distribution of energy states are available. These energy states can be occupied by thermalized electrons resulting in broad thermal distribution of electrons around Fermi level of metals. This thermal distribution of electrons results in thermal broadening of IETS peaks. This reduces the resolution of IETS at room temperature.

The objective of this work is to develop "electron energy filters" to narrow down the thermal energy distribution of electrons at room temperature. Quantum dots due to their small size have discrete energy levels. So even though electrons in quantum dots can possess thermal energy at room temperature, they can only occupy the discrete energy states available in quantum dots. Hence, the thermal energy distribution of electrons can be narrowed down to only energy levels available in quantum dots. In other word, quantum dots act as electron energy filter to narrow down

thermal distribution of electrons.

1.4 Scope of Thesis

In my thesis, I first discuss fabrication and characterization of inelastic electron tunneling devices.

Chapter 2, describe fabrication of metal-insulator-metal inelastic tunneling devices. As we know, inelastic electron tunneling spectroscopy involves direct measurement of $\frac{d^2I}{dI^2}$. Chapter 3, describes the instrumentation developed to directly measure $\frac{d^2I}{dI^2}$ using standard modulation technique. This system is named as inelastic electron tunneling spectrometer. In order to determine the required electron energy filtering, to resolve vibrational energy levels of molecules using IETS, thermal broadening of IETS peaks is studied. Chapter 4, discuss theoretical prediction of thermal broadening and compares it with observed IETS peak-width at various temperatures.

Once the required electron energy filtering (i.e Q-factor of energy filter) is determined, electron energy filters are designed using quantum dots. Chapter 5, discuss the theoretical model of a 2dimensional array of quantum dots that can be used as electron energy filters. This $2D$ array of QDs is modeled as a resonant tunneling diode with minibands. Chapter 6, presents fabrication of quantum dots energy filters using *CdSe* QDs. These filter consist of $ITO - Al_2O_3 - CdSeQDs - Pb$ and $Al - Al_2O_3 - CdSeQDs - Pb$ device structure. Current-voltage measurement is performed on these devices to determine the Q-factor (i.e. extent of energy filtering) of these *CdSe* QDs energy filters.

Chapter 7, describes using single *CdSe* QDs for electron energy filters. Current-sensing atomic force microscopy in IV spectroscopy mode is used to study the electron transport through single QDs at room temperature. This current-voltage measurement is then used to determine Q-factor of single *CdSe* QDs energy filter.

Finally, Chapter 8 compares the electron energy filtering required to perform high resolution inelastic electron tunneling spectroscopy obtained from Chapter 4 with achievable energy filtering using array of *CdSe* QDs (Chapter 6) and single *CdSe* QDs (Chapter 7). My thesis conclude with

discussing highest resolution achievable using quantum dots energy filter and suggest future work relating to further improving the resolution of inelastic electron tunneling spectroscopy at room temperature.

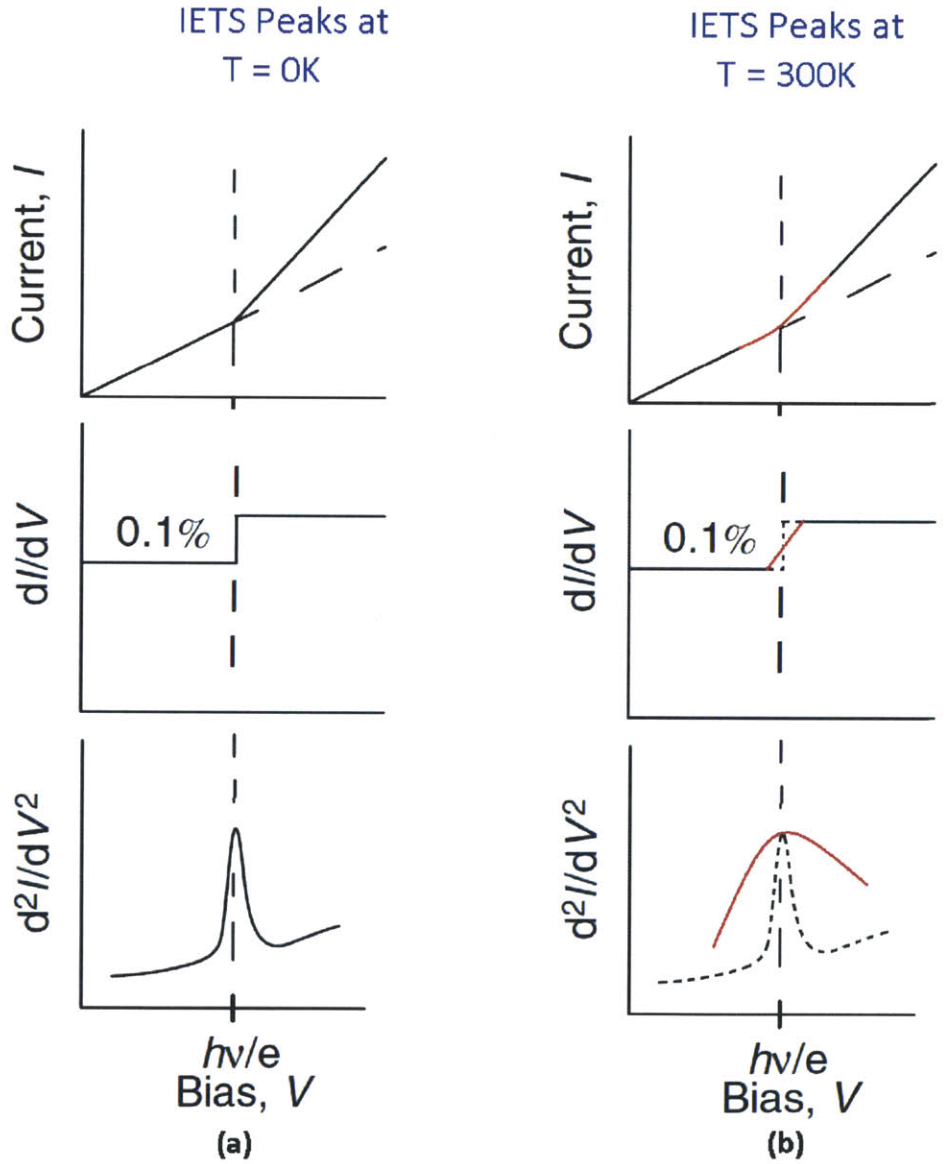

Figure 1.5: Schematic representation of change in conductance of $M-I-A-M$ devices and observation of IETS Peaks

Chapter 2

Fabrication of $Al - Al_2O_3 - HCOOH - Pb$ Tunneling Device

Tunneling device fabricated for inelastic electron tunneling spectroscopy consist of $Al - Al_2O_3 - HCOOH - Pb$ structure schematically shown in figure 2.1. For bottom electrode, aluminum is

Figure 2.1: Schematic diagram of Metal-Insulator-Metal Inelastic Tunneling Device

used as it is easy to grown aluminum oxide which acts as tunneling barrier. For top electrode, various metals were tried such as *Au*, *Ag* , *Al* before settling on *Pb*. Metal such as *Au*, *Ag* , *Al* have small atomic size and high kinetic energy at room temperature and diffuse through aluminum oxide. On the other hand *Pb* has large atomic size and does not diffuse through aluminum oxide. The molecules under study is introduced into the tunneling junction during the fabrication of the device. Various methods for introducing molecules into the tunneling junction such as infusion doping, spin coating and vapor exposure is studied.

2.1 Substrate Cleaning

Standard microscope glass substrate is cut into small pieces of dimension $10mmx10mm$. Following cleaning procedure is performed to remove organic impurities and dust from the substrate.

1. Substrate is cleaned with acetone in ultrasonic bath for $60s$ to remove organic impurities.
2. Before acetone dries out, its washed away with isopropyl alcohol.
3. The substrate is then rinsed thoroughly with DI water and dried by blowing clean nitrogen.
4. These substrate are then tested for low temperature tolerance by quickly immersing them on liquid nitrogen. Those pieces which were cracked during immersion were discarded and rest are used for device fabrication.

2.2 Aluminum Deposition

Aluminum is deposited using Auto 306 thermal evaporation system. In order to deposit $1mm$ wide aluminum strip on glass substrate, shadow mask is used. The deposition system consist of turbo-molecular pump backed by rotary pump to create high vacuum. An alumina coated tungsten boat is used to melt aluminum to avoid formation of aluminum-tungsten alloy. The system is also fitted with thickness meter to measure the thickness of the deposited metal. For deposition, the deposition chamber is first evacuated to base pressure of $3x10^{-6}mbar$ and then deposition is started at $1nm/s$ rate to deposit $100nm$ thick Al layer.

2.3 Growth of Aluminum Oxide

Aluminum oxide is grown on top of Al electrode using "exposure to air at room temperature" and "plasma oxidation" process. For room temperature exposure, sample is kept in room temperature in lab environment for 24 hours. These method grows native aluminum oxide with oxide thickness of around $\sim 4nm$. The disadvantage of growing oxide using this method is as follows

1. The oxide grown using this technique is contaminated with atmosphere impurities.

2. Grown aluminum oxides are not very dense and possess few pin holes. These pin holes leads to shorting of the two metal electrodes destroying the devices. The success rate of devices fabricated using this method is very low.

3. The devices take long time to fabricate and its difficult to fine control the thickness of the grown aluminum oxide. Devices fabricated using this method suffer from poor reproducibility.

The other method which gave very good quality dense oxide, free from pin holes and impurity is grown using oxygen plasma. This method is described in next section.

2.3.1 Growth of Aluminum Oxide using Oxygen Plasma

Anatech SP-100 plasma cleaner is used to grow aluminum oxide. The plasma chamber is connected to an oxygen cylinder through a flow controller. The advantage of using this system is that the oxide is very dense and is free from impurities. The thickness of grown oxide is controlled by controlling Rf power, oxygen flow rate in plasma chamber and time of growth. The resistance of the device depends upon the thickness of aluminum oxide and is used as quantitative estimate for thickness of grown aluminum oxide. First, several samples are prepared by depositing $100nm$ of Al on pre-cleaned glass substrate. Aluminum oxide is grown using different experimental parameters such as Rf power, oxygen flow rate and time of growth. After the growth of a aluminum oxide, $200nm$ Pb is deposited in cross electrode geometry perpendicular to aluminum electrode. For making electrical contacts, indium soldering is used as it has very high affinity to glass. Once the contacts are made, device resistance is measured using Agilent $34401A$ multimeter. Table2.1 tabulates various growth parameters and observed resistance of fabricated devices.

Current-voltage measurement is taken using HP semiconductor analyzer. Figure shows a current-voltage characteristics of an $Al - Al_2O_3 - Pb$ device.

Power	Flow (sccm)	Time (Sec)	Resistance Ω
50	10	10	45.3K
50	10	60	0.6M
50	1	10	3.1K
50	1	60	28.2K
10	10	10	10.7K
10	10	60	51K
10	1	10	1K
10	1	60	14.2K

Table 2.1: Growth of Al_2O_3 with different experimental parameters

Using the data in table 2.1, it is concluded that the optimum condition to grow aluminum oxide of desired thickness and desired device resistance ($\sim 1K$) is, Rf power of $10W$, oxygen flow-rate of $1sccm$ and oxide growth time of $10s$.

2.4 Doping of Aluminum Oxide

For the doping of Al_2O_3 with impurity, the samples are kept in air for $\sim$ 20 hours after the oxide growth. It is believed that impurities got introduced in Al_2O_3 using this period. For doping aluminum oxide with $HCOOH$, freshly grown aluminum oxide sample and $5ml$ of $HCOOH$ in a container is kept in an vacuum chamber. The chamber is then pumped to a base pressure of $10^{-3}mbar$. After keeping the sample in the chamber for about $10min$ the chamber is purged with nitrogen and Pb is deposited on top of doped aluminum oxide.

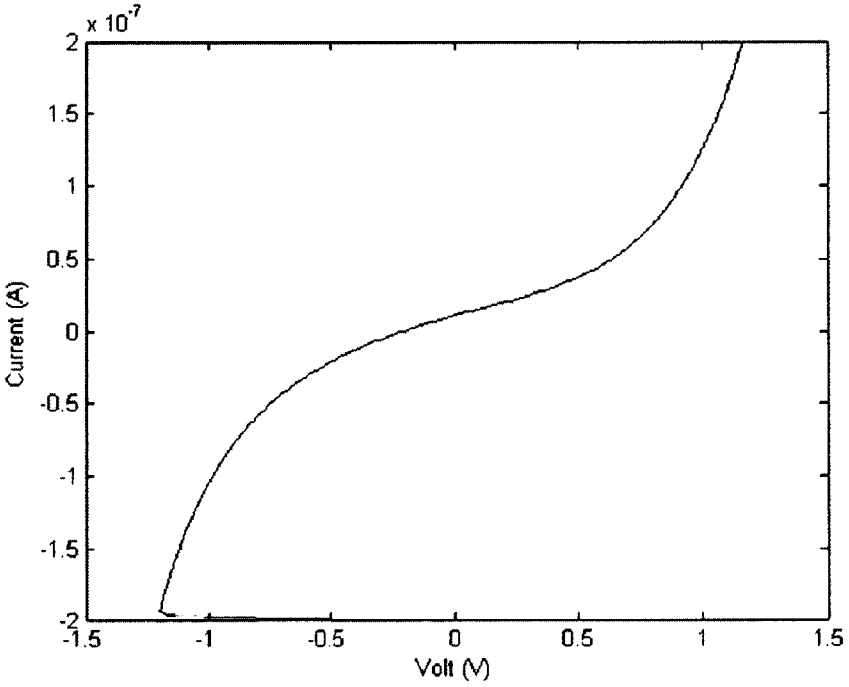

Figure 2.2: Current-Voltage Characteristics of an $Al - Al_2O_3 - Pb$ Device

Chapter 3

Inelastic Electron Tunneling Spectrometer

Inelastic electron tunneling spectroscopy requires measurement of second derivative of current-voltage characteristics. Instrumentation is developed to measure second derivative of I-V curve using standard modulation technique. An AC/DC current source is used to bias the device under study. The DC voltage across the device is measured using Keithley 2182S nanovoltmeter. For measurement of first and second derivative of current w.r.t voltage, two digital lock-in amplifiers are used. This chapter first discuss theory of modulation technique used for direct measurement of $\frac{d^2I}{dV^2}$ followed by describing actual instrumentation used for measurement. Chapter concludes with presenting measurement inelastic tunneling spectra of $Al - Al_2O_3 - HCOOH - Pb$ device fabricated in last chapter.

3.1 Theory of IETS Spectrometer Design

Consider a dc current I_b modulated with small ac current $icos(\omega t)$, is allowed to pass through the device. The total current through the device is $I = I_b + icos(\omega t)$ and the voltage drop is $V_D(I)$. The Taylor series expansion of the voltage across the device $V(I)$ about the dc bias current I_b is given by

$$V_D(I) = V(I_b) + \left(\frac{dV}{dI}\right)(I - I_b) + \left(\frac{1}{2}\right)\left(\frac{d^2V}{dI^2}\right)(I - I_b)^2 + ...$$

$$\Rightarrow V_D(I) = V(I) + \left(\frac{dV}{dI}\right) icos(\omega t) + \left(\frac{1}{2}\right)\left(\frac{d^2V}{dI^2}\right)[icos(\omega t)]^2 + ...$$

$$\Rightarrow V_D(I) = V(I) + \left(\frac{dV}{dI}\right) icos(\omega t) - \left(\frac{1}{4}\right)\left(\frac{d^2V}{dI^2}\right) i^2 cos(2\omega t) + ...$$

Now, lock-in amplifiers tuned at ω and 2ω will respectively measure (rms values)

$$V_\omega = \frac{1}{\sqrt{2}}\left(\frac{dV}{dI}\right) i$$

$$V_{2\omega} = -\frac{1}{\sqrt{2}}\left(\frac{1}{4}\right)\left(\frac{d^2V}{dI^2}\right) i^2$$

Once we have the value of $\left(\frac{dV}{dI}\right)$ and $\left(\frac{d^2V}{dI^2}\right)$, IETS signal $\frac{d^2I}{dV^2}$ can be calculated using the following relation

$$\frac{d^2I}{dV^2} = -\left(\frac{d^2V}{dI^2}\right)\left(\frac{dI}{dV}\right)^3$$

If we assume that the bias voltage is limited to $0.5V$ then the value of $\left(\frac{dI}{dV}\right)$is constant and above equation can be reduced to

$$\frac{d^2I}{dV^2} = -k\left(\frac{d^2V}{dI^2}\right)$$

Since in such cases, $\left(\frac{d^2I}{dV^2}\right)$ and $\left(\frac{d^2V}{dI^2}\right)$ are qualitatively same, in our reported data we have

directly plotted the value of $\left(\frac{d^2V}{dI^2}\right)$ or voltage $V_{2\omega}$ measured from lock-in amplifier tuned at frequency 2ω

3.2 Design of IETS Spectrometer

The simplified schematic circuit diagram of IETS spectrometer is shown in figure 3.1 . For ap-

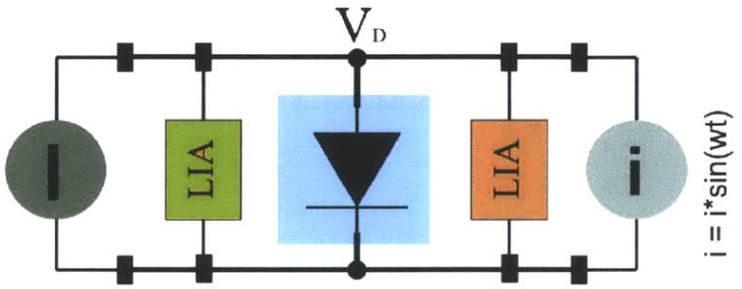

Figure 3.1: Schematic circuit diagram of IETS Spectrometer

plying both AC and DC current source, Keithley 6221 AC/DC current source is used. In order to measure DC voltage Keithley 2182A nanovoltmeter is connected to buffered output of Keithley 6221 AC/DC current source. For measuring V_ω and $V_{2\omega}$, two digital lock-in amplifier (with high common mode rejection ration) from Stanford research system model no. SR830 and SR850 are used which are respectively tuned for ω and 2ω frequency.

Figure 3.2 shows the block diagram of IETS spectrometer showing the connection of various instruments. All the instruments are controlled by a program written in matlab through GPIB interface. Since in some devices, junction resistance is of the order of metal lead resistance, 4-probe measurement technique is used. Lock-in amplifiers are chosen to operate at a relatively low frequency i.e. less than $50Hz$. A low frequency is chosen for several reasons such as

1. Getting far enough below the frequency roll-off of the device under test (DUT) and interconnects for an accurate measurement

2. Avoiding noise at the power line frequency, and

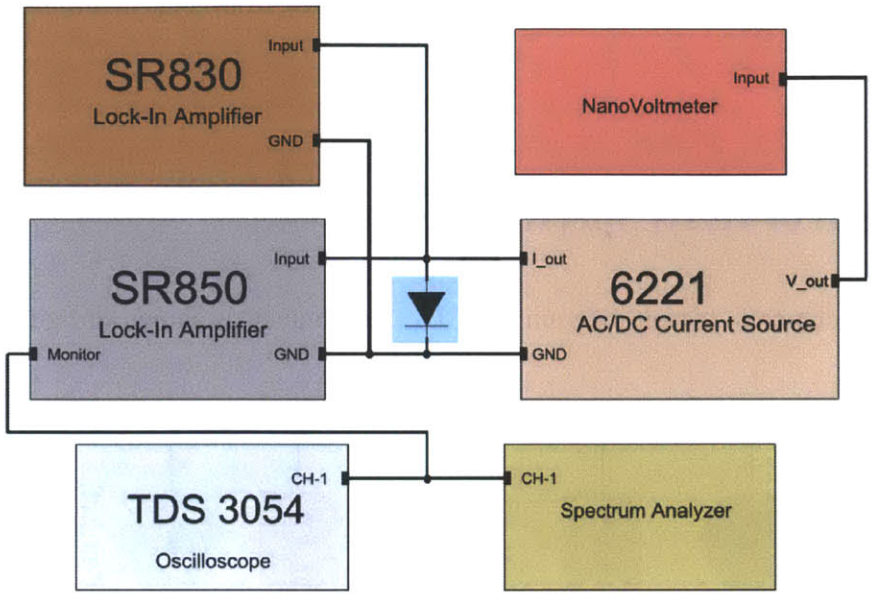

Figure 3.2: Block diagram of IETS spectrometer design

3. Getting below the frequency cutoff of in-line electromagnetic interference (EMI) filters added to keep environmental noise from reaching the device under test (DUT).

The quality of the data largely depends upon the time constants used in lock-in amplifiers. It takes 5 time constant to stabilize the reading of lock-in amplifier. The capacitance of cable and the device must be considered while calculating the time constant RC. The tunneling diode acts as a combination of resistor and a capacitor connected in parallel. For a tunneling diode with resistance of $100ohm$ and capacitance $\sim 0.3uF$, calculated time constant is $T_C = RC = 30uSec$ but for $10K$ device with capacitance $12nF$, $T_C = RC = 120us = 0.1ms$. There is also a settling time for current from 6221 to settle, its usually $100usec$ and must be considered while deciding the time constant for lock-in amplifiers. Although, large time constants Tc give good signal to noise ration, such measurement takes much longer time complete and suffer from $1/f$ noise.

Care must be taken to not to over-drive lock in amplifiers. If an amplifier is over-driven, the output signal clips because the amplifier is saturated. The output signal is no longer a pure sinusoid, and harmonics are present at multiples of the input frequency. In such case, the Lock-in amplifier set to measure second harmonics will not measure the second derivative but the signal due to

saturation of amplifier.

3.3 Inelastic Electron Tunneling Spectra of $Al-Al_2O_3-HCOOH-Pb$ Device

This section briefly describes fabrication of $Al-Al_2O_3-HCOOH-Pb$ devices and presents inelastic electron tunneling spectra obtained from devices. For fabricating $Al-Al_2O_3-HCOOH-Pb$ devices, first the substrate is cleaned as described in section 2.1. $100nm$ aluminum is deposited followed by oxygen RF-plasma oxidation at $10sccm$ oxygen flow rate, $10W$ RF power for $10s$. The device is then kept in air for ~$20h$ before exposing it to $HCOOH$ vapor for oxide doping. Final resistance of the device is found be around $\sim 1K$. For IETS measurement, electrical contacts are made using indium solder and the sample is mounted inside the liquid helium cryostat.

Figure 3.3 shows the current-voltage characteristics of $Al-Al_2O_3-HCOOH-Pb$ devices. For direct measurement of $\frac{dV}{dI}$ and $\frac{d^2V}{dI^2}$, instrumental setup described in previous section 3.2 is used. Modulation voltage of typically of the order of $1mV$ (or 10 wave number) is used for AC modulation. For comparison purpose $\frac{dV}{dI}$ is also computed numerically using. Figure 3.4 shows the first derivative of voltage w.r.t current i.e. $\frac{dV}{dI}$ of $Al-Al_2O_3-HCOOH-Pb$ devices. The blue curve is direct measurement of first derivative and the red curve is computed first derivative using current-voltage measurement. As it can be seen in figure 3.4, there is large noise in calculated first derivative as compared to measured first derivative. Calculating second derivative with noisy computed first derivative is not of any use as all the noise in first derivative will blow up in second derivative. Hence, the instrumentation is developed for direct measurement of the second derivative.

Figure 3.5 shows plot of second derivative of voltage w.r.t current i.e. $\frac{d^2V}{dI^2}$ vs voltage. As it can be seen in figure 3.5, IETS peaks are observed in the $\frac{d^2V}{dI^2}$ w.r.t current plot and can be identified as the vibrational energy level of the impurity molecules in the tunneling junction. Table 3.1 tabulate the position of the observed peak and the identified mode of energy associated with these peaks.

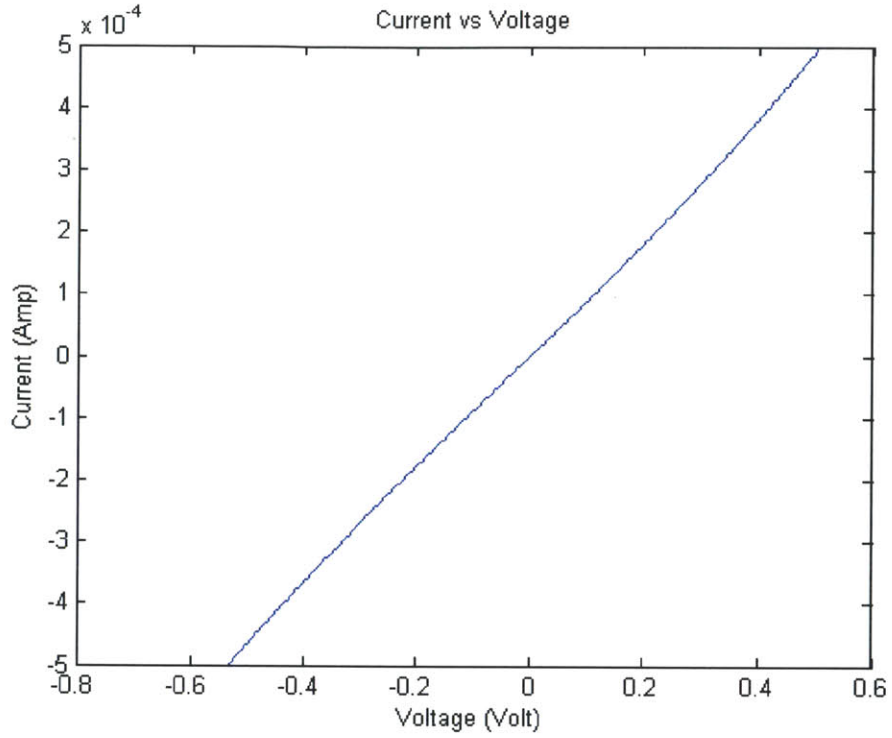

Figure 3.3: Current-Voltage Characteristics of $Al - Al_2O_3 - HCOOH - Pb$ Devices

It must be noted that these peaks are only visible at low temperature and disappear at room temperature. For comparison, figure 3.6 shows the second derivative of voltage w.r.t current i.e. $\frac{d^2V}{dI^2}$ plot for $4.2K$ and $300K$. As described in chapter 1, IETS peaks broadens due to thermal distribution of electrons in metals and hence no IETS peaks are observable at room temperature. In next chapter, thermal broadening of IETS peaks is studied in great detail.

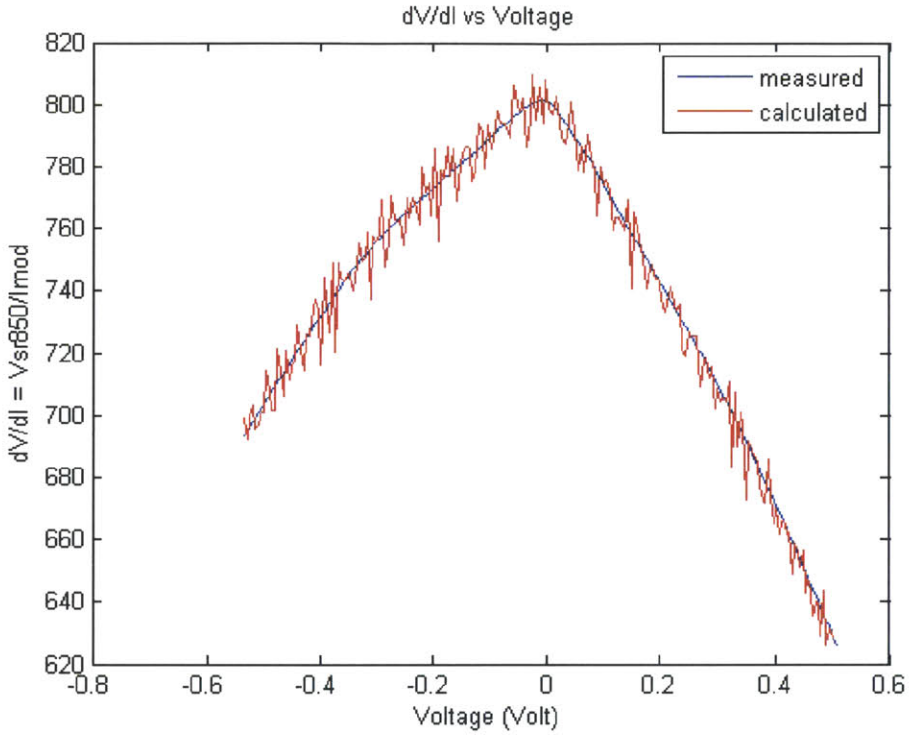

Figure 3.4: Firs derivative $\frac{dV}{dI}$ measured for $Al - Al_2O_3 - HCOOH - Pb$ Devices

S.No.	Peak Position (mV)	Energy (cm^{-1})	Identified Mode
1	112	903	$O-H$ Bend
2	178	1435	$C-H$ Bend
3	361	2911	$C-H$ Stretch
4	438	3532	$O-H$ Stretch

Table 3.1: Peak position and corresponding identified vibrational mode for impurities in $Al - Al_2O_3 - HCOOH - Pb$ Devices

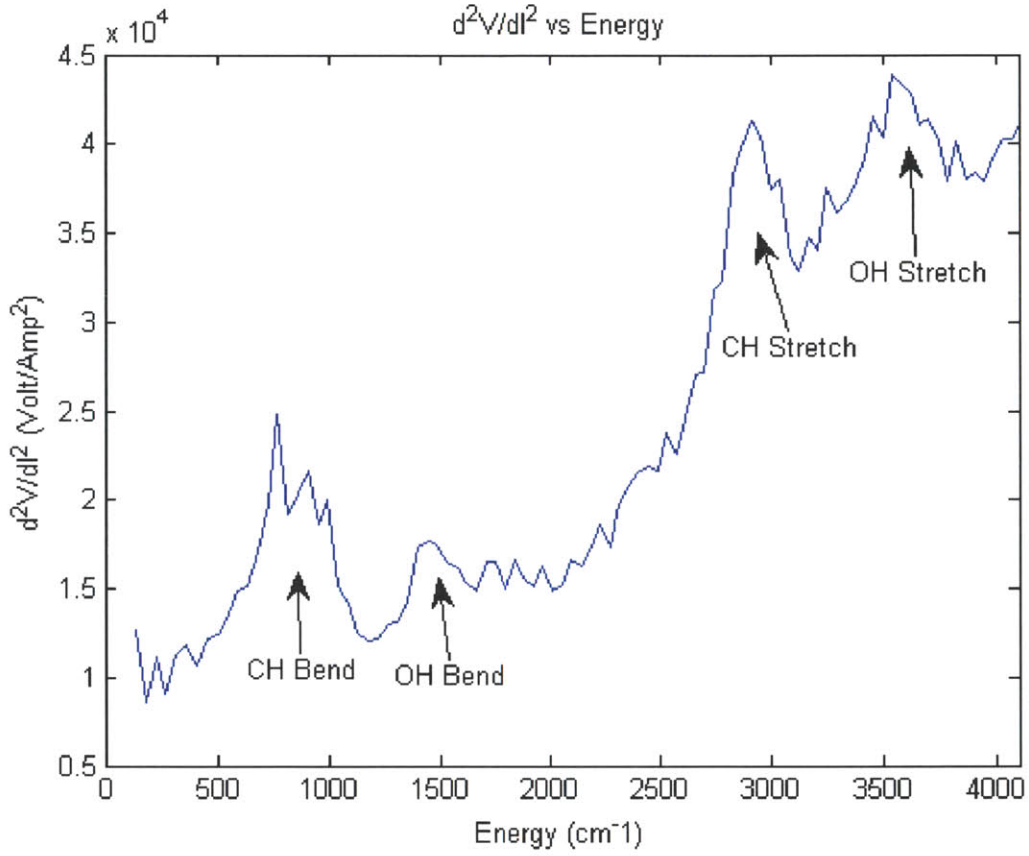

Figure 3.5: Measured IETS peaks on $Al - Al_2O_3 - HCOOH - Pb$ Devices

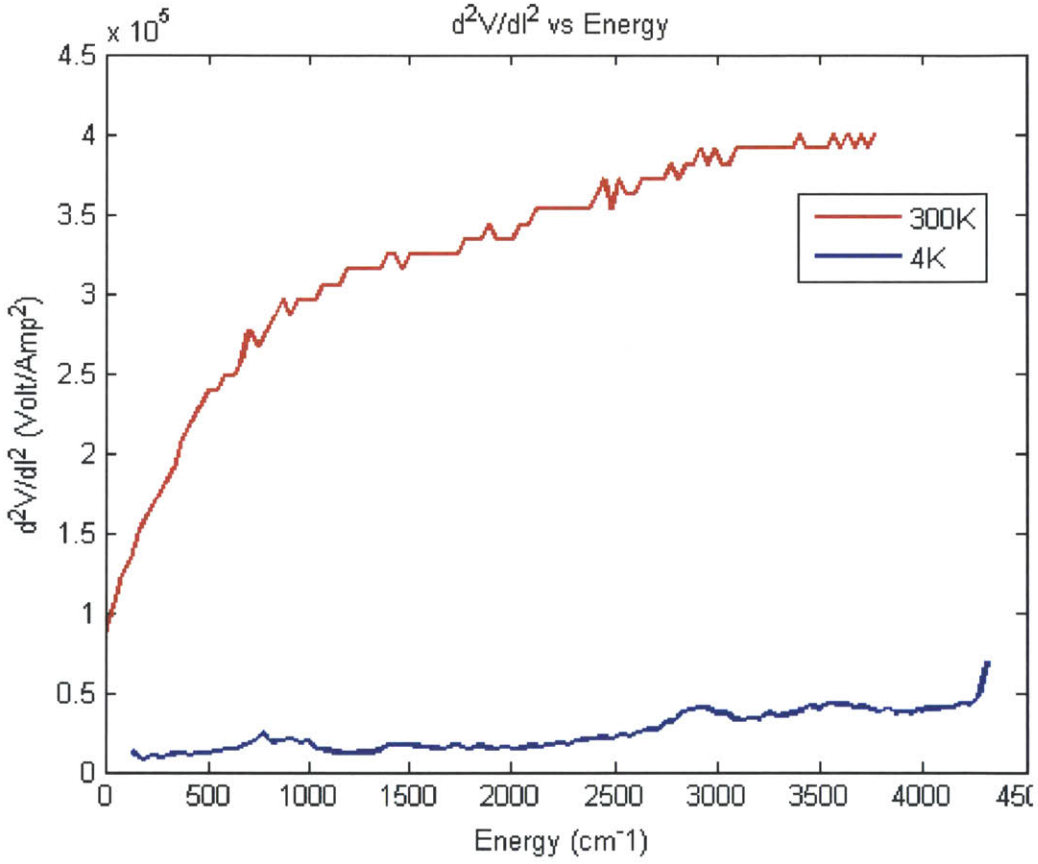

Figure 3.6: $\frac{d^2V}{dI^2}$ w.r.t current plot of $Al - Al_2O_3 - HCOOH - Pb$ devices at low temperature and room temperature

Chapter 4

Thermal Broadening of IETS Peaks

One major limitation of application of inelastic electron tunneling spectroscopy as an e-nose is that it should be performed at very low temperature typically $\sim 4.7K$. At room temperature, due to thermal smearing of the electrons in metals, broad line-width of IETS peaks are observed. This phenomena is called "thermal broadening of IETS peaks". To understand this, one has to compare the band diagram of $metal - insulator - metal$ device at cryogenic temperature and at room temperature. Metals have continues distribution of electron energy density of states given by

$$\rho(E) = \frac{4\pi(2m)^{(3/2)}}{h^3}\sqrt{E}$$

The conduction electron population for a metal is given by multiplying the density of conduction electron states $\rho(E)$ times the Fermi function $f(E)$. The number of conduction electrons per unit volume per unit energy is

$$\frac{dn}{dE} = \frac{4\pi(2m)^{(3/2)}}{h^3}\sqrt{E}\frac{1}{e^{(E-E_F)/kT}-1}$$

At $T = 0$, the Fermi function is a step function and electrons only occupy energy levels up-to Fermi level. At room temperate, electrons have energy $kT \sim 25mV$ and occupy energy levels above the Fermi level. Figure 4.1

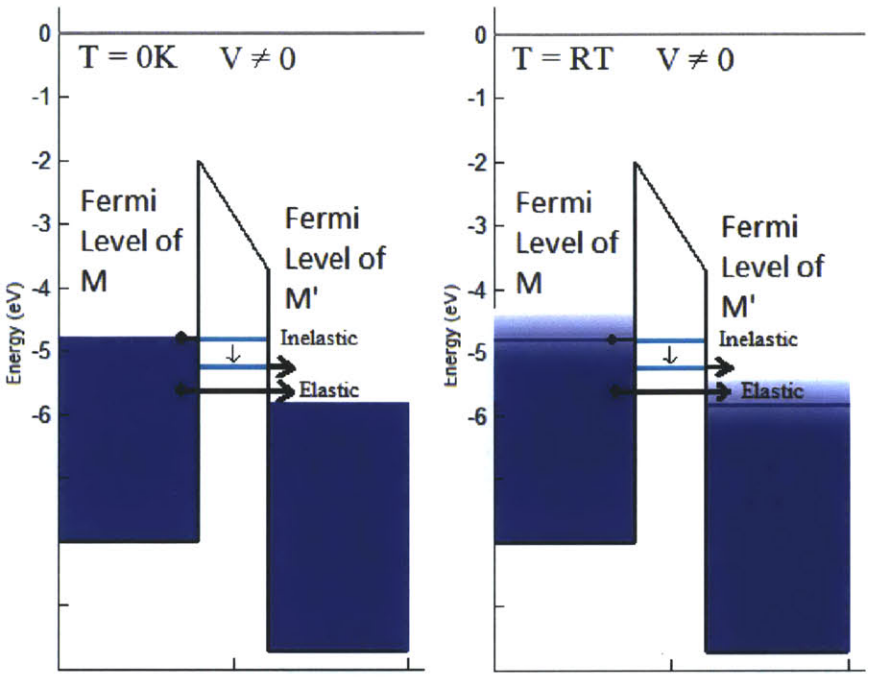

Figure 4.1: Band diagram of $metal - insulator - metal$ devices at low temperature and at room temperature

band diagram of $metal - insulator - metal$ device at cryogenic temperature and at room temperature. At room temperature since there is broad distribution of energy levels of electrons, the process of addition of inelastic tunneling electron is not very sharp. Hence the observed IETS peaks have broad peak width. Next section derives the relationship between IETS peak-width and temperature.

4.1 Theory of Thermal Broadening of IETS Peaks

Inelastic current through the junction is give by [10]

$$I(V) = C\int_{-\infty}^{\infty} dE\,\{f(E)[1-f(E+eV-\hbar\omega_0)]\}\,xN_1(E)N_2(E+eV-\hbar\omega_0)$$

where,

- C is a constant which takes into account all the various tunneling parameters which are inde-

pendent of E and T

- f(E) is the Fermi function for metals

- $N_1(E)$ and $N_2(E)$ are effective tunneling density of states

- V is applied bias voltage

- $\hbar\omega_0$ is vibrational energy of the molecule

Since, $N_1(E)$ and $N_2(E)$ which are effective tunneling density of states are equal to unity for normal metal and $f(E) = \frac{1}{1+e^{E/kT}}$, above equation will reduce to

$$I(V) = C\int_{-\infty}^{\infty} dE \left(\frac{1}{1+e^{E/kT}}\right)\left(1 - \frac{1}{1+e^{[E+e(V-V_0)]/kT}}\right)$$

Solving above equation we get,

$$I(V) = Ce(V-V_0)\frac{e^{e(V-V_0)/kT}}{e^{e(V-V_0)/kT}-1}$$

differentiating above equation w.r.t V twice we get

$$\frac{d^2I}{dV^2} = C\frac{e^2}{kT}\left[e^v \frac{(v-2)e^v+(v+2)}{(e^v-1)^3}\right]$$

where $v = \frac{e(V-V_0)}{kT}$. Above equation gives $\frac{d^2I}{dV^2}$ as a function of $(V-V_0)$. Plotting $\frac{d^2I}{dV^2}$ w.r.t $(V-V_0)$, FWHM is give by $5.4kT$. If W_0 is the actual peak width at $T=0$ than

$$W(T) = \sqrt{(5.4kT)^2+W_0^2}$$

Next section discuss the experimental results on thermal broadening of IETS peaks in $Al-Al_2O_3-HCOOH-Pb$ devices.

4.1.1 IETS Peak-width at Various Temperature

Thermal broadening of IETS peaks are empirically measured to estimate the order of electron energy filtering is required. A <model number> temperature controller is attached to the cryostat to change the temperature to desired value. PID parameters in temperature controllers is set so that the temperature is stable up-to $100mK$. The device is first brought to desired temperature and then IETS measurement is performed. To obtain usable second derivative at high temperature, modulation voltage of $10mV$ is used.

Figure 4.2 and figure 4.3 shows inelastic electron tunneling spectra of $Al-Al_2O_3-HCOOH-Pb$ device at $T=4.2K$, $T=10K$, $T=30K$, and $T=77K$ respectively. As the temperature at which the sample is increased, the lines broaden and the peak height decreases. For $-CH$ stretch, at$4.2K$ the line-width is about $19.8mV$, but at 77'K the line-width is about$46.2mV$. At room temperature the broadening is too great to get any reasonable estimate of line-width. It must be noted that the peak width also depends upon the modulation voltage bias used, actual impedance of the device and if one of the metal is super conducting.

To study the variation of peak width w.r.t temperature two IETS peaks corresponding to $-OH$ bend and $-CH$ stretch is used. Table 4.1 tabulates peak-width of peak observed for $-OH$ bend

Temperature	Peak-width of$-OH$ band (mV)	Peak-width for$-CH$ stretch (mV)
$4.2K$	14.8	19.8
$10K$	15	20.2
$30K$	16.6	24.1
$77K$	-	46.2

Table 4.1: IETS peak-width w.r.t. temperature

and $-CH$ stretch at various temperature. Figure 4.4 shows the variation of IETS peak width for $-CH$ stretch with temperature. Fitting function

$$W(T)=\sqrt{(5.4kT)^2+W_0^2}$$

is used to best-fit the data in order to determine absolute peak width W_0. The calculated value of

W_0 is found to be $19.4mV$.

Similarly, for $-OH$ bend peak, variation of peak width with respect to temperature is shown in figure 4.5 . After best fitting the curve the value of absolute peak is found to be $W_0 = 14.5mV$. This peak simply disappeared at $77K$ and hence only three points are used for curve fitting. When temperature of sample is increased, this results in broadening of IETS peaks. At a certain temperature, the peaks are so broad that, different vibrational energy modes of molecules under study can not be resolved. Next section determine this maximum characteristic temperature and energy distribution of electrons associated with this temperature.

4.2 Maximum Temperature to Resolve IETS peaks

In order to resolve IETS peaks, the peak-width (FWHM) should be at least of the order of distance between two consecutive peaks. As shown in table 3.1, the difference in energy of $-OH$ and $-CH$ bend is of the order of $\sim 50mV$. Hence in order to distinguish between these two peaks, the peak-width should at least be of the order of $\sim 50mV$. From figure 4.4 we know, in order to get peak width of $50mV$ the experiment should be performed at a temperature not higher than $77K$. Hence the maximum temperature at which $HCOOH$ peak can be observed is $T_{max} \sim 77K$. (It must be noted that the value of T_{max} depends upon the molecule under study. For some molecule if the difference between individual vibrational energy level is of the order of $\sim 20mV$ than T_{max} will be around $\sim 10K$)

Now for $T_{max} = 77K$, thermal energy of electrons in metals are $6.6meV$. In order to perform IETS spectroscopy at room temperature, the required electron energy filtering should be of the order of $\sim 6.6meV$. Next chapter describes the theoretical study of using quantum dots as electron energy filters for this application.

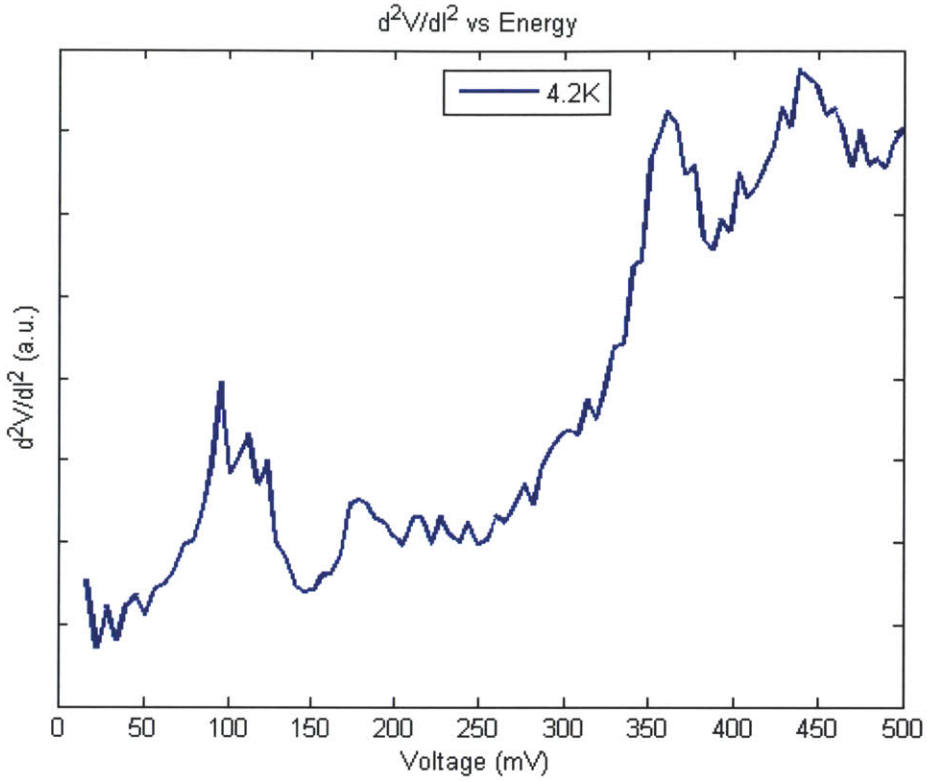

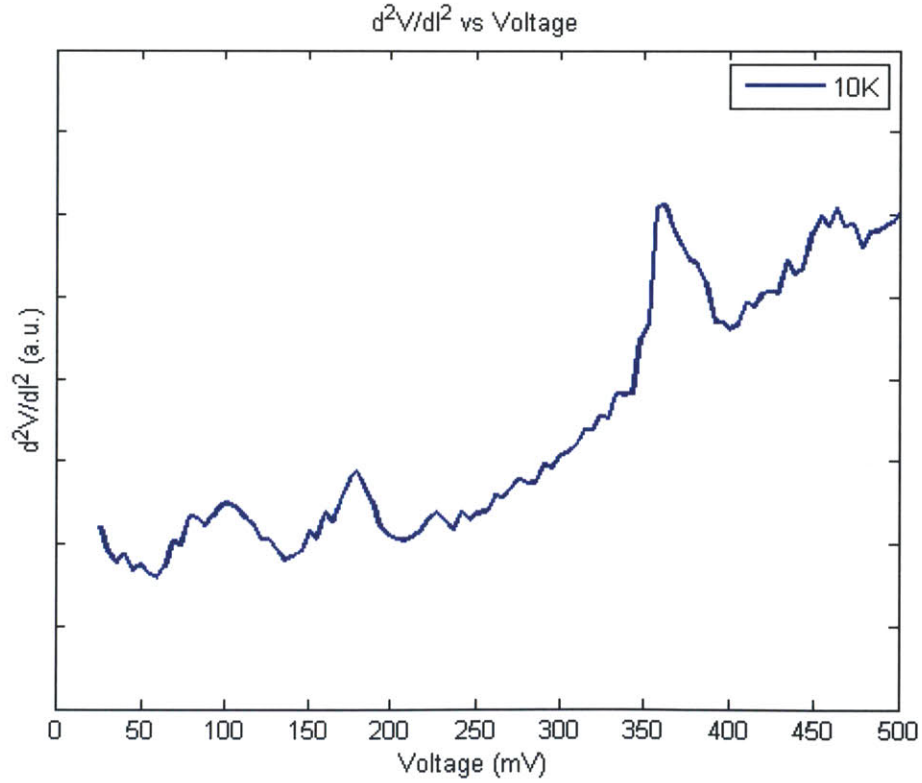

Figure 4.2: Measured IETS peaks on $Al - Al_2O_3 - HCOOH - Pb$ Devices at $T = 4.2K$ and $T = 10K$

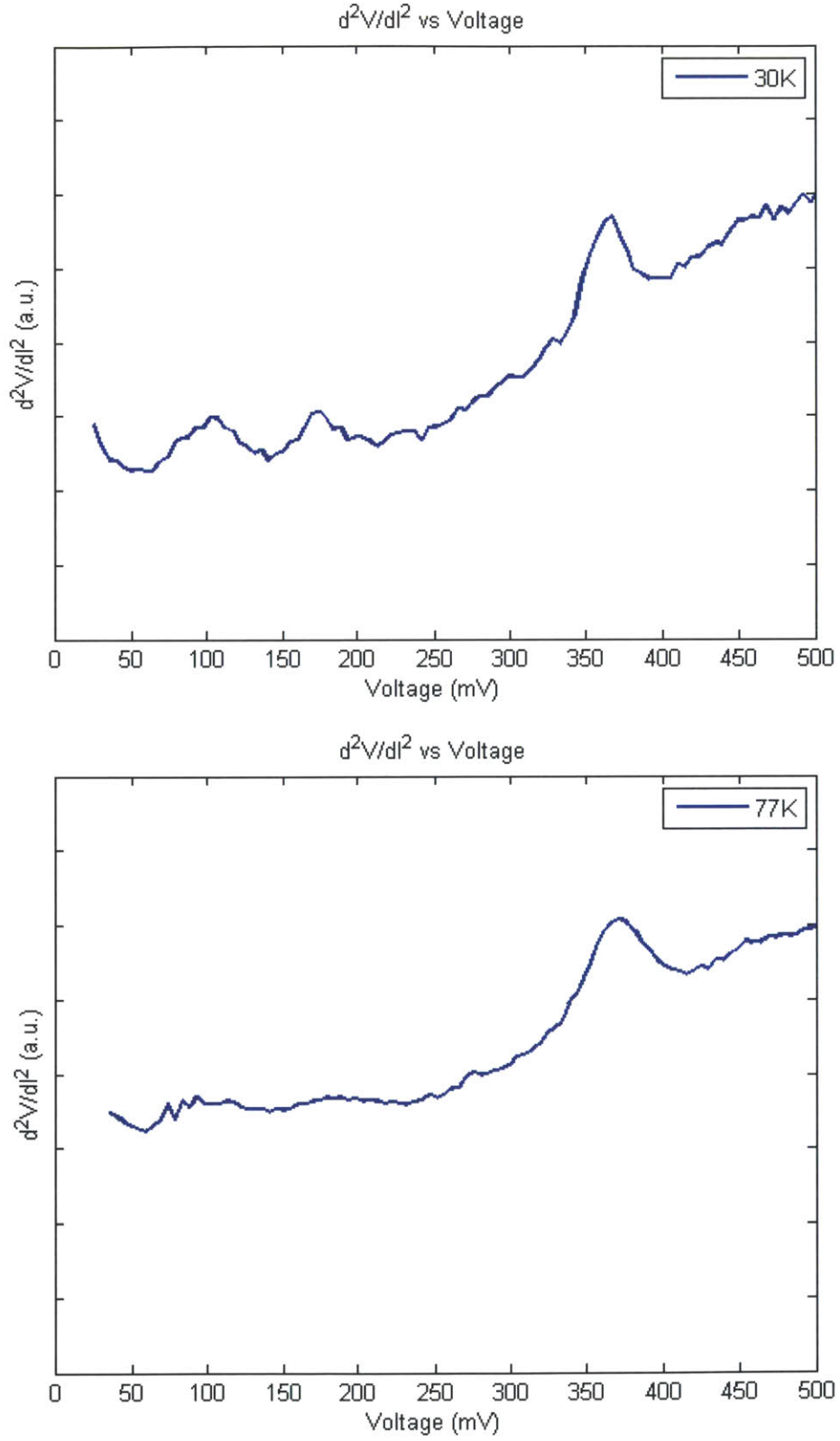

Figure 4.3: Measured IETS peaks on $Al - Al_2O_3 - HCOOH - Pb$ Devices at $T = 4.2K$ and $T = 10K$

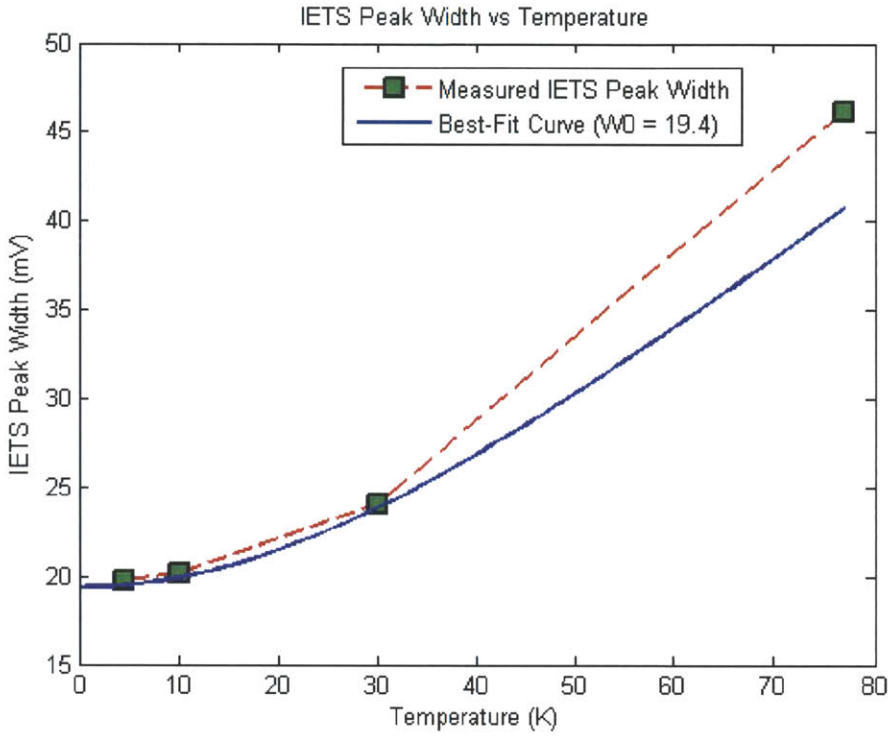

Figure 4.4: Plot of IETS peak width (W) w.r.t. Temperature for $-CH$ stretch peak

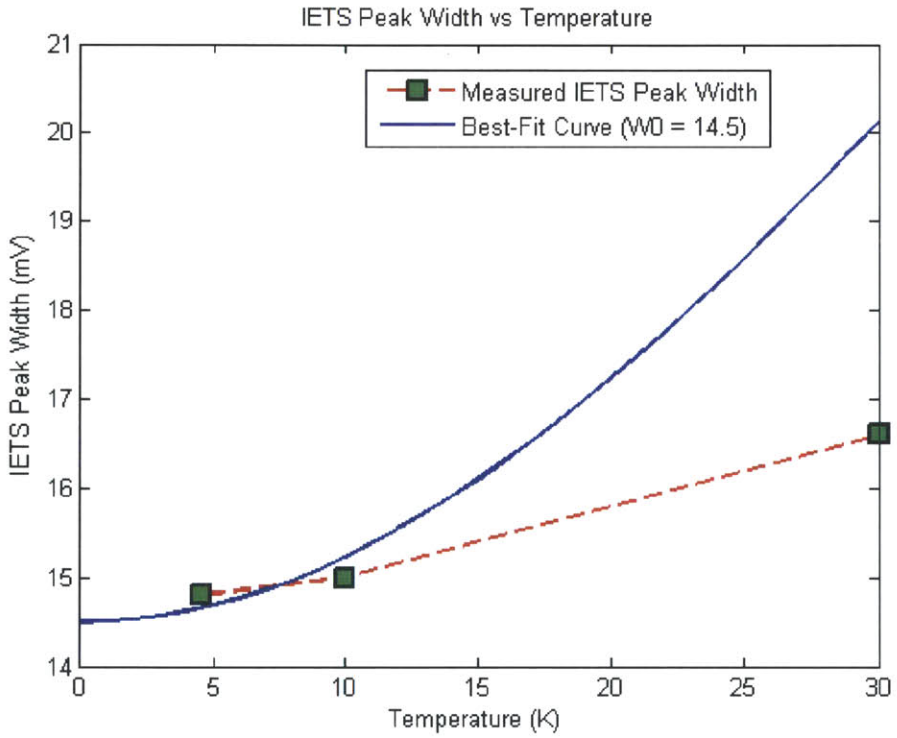

Figure 4.5: Plot of IETS peak width (W) w.r.t. Temperature for $-OH$ band peak

Chapter 5

Theory of Quantum Dots Electron Energy Filters

This chapter investigate resonant tunneling through 2-dimentional quantum dot arrays which is transverse to the direction of tunneling current. This system can be modeled as a potential double barrier, incorporating a periodic quantum dot structure with the periodicity in the direction perpendicular to the tunneling current. It is assumed that periodic potential is infinitely spread in the plane of the barrier. The periodic array of quantum dots perpendicular to tunneling current is modeled as thick quantum well whose $\delta - function$ is modulated periodically in transverse direction[11]. Thus the potential profile of this system can be written as

$$U(x,y) = -V_0 \delta(x) f(y)$$

where, $f(y) > 0$ is a periodic potential in transverse direction. Assuming that the modulation function $f(y)$ is week, using the adiabatic approximation the wave function can be written as:

$$\Phi(x,y) = \eta(y) \Psi_y(x)$$

The Schrodinger equation can be then written as:

$$-\frac{\hbar}{2m}\frac{\partial^2}{\partial x^2}\Psi_y(x) - V_0\delta(x) f(y)\Psi_y(x) = E(y)\Psi_y(x)$$

The solution of above equation is eigenfunction $\Psi_y(x)$

$$\Psi_y(x) = \sqrt{\kappa_0} exp(-\kappa_0[x])$$

where, $\kappa_0 = \frac{V_0 f(y) m}{\hbar^2}$ and eigen energy state

$$E_0 = -\frac{mV_0^2 f^2(y)}{2\hbar^2}$$

The system can be considered as a resonant tunneling diode (figure5.1) with mini band width $4\triangle$ and energy $\varepsilon_{1k} = E_0 + \triangle(2 - cosk_g b - cosk_z b)$, where b is the period of quantum dots and E_0 is the energy difference between the Fermi-level of metal and first mini-band in quantum dot arrays. The energy band due to transverse energy is given by $\varepsilon_{2k} = E_0 + U + \triangle_1(cosk_y b + cosk_z b)$, where $U - 2\triangle_1$ is the gap between the two minibands. In Aluminum and Lead electrodes, energy of electrons are give by

$$E_{Al} = \frac{\hbar^2 k^2}{2m_{Al}}$$

$$E_{Pb} = \frac{\hbar^2 k^2}{2m_{Pb}}$$

where $m_{Al}$and $m_{Pb}$is effective electron mass in aluminum and lead respectively

The current through this double barrier resonant tunneling system consist of both elastic and inelastic tunneling current. These are discussed next

5.1 Current-Voltage Characteristics of QDs Array

The current through the 2-dimentional array of QDs sandwiched between two metal electrodes consist of both elastic tunneling electrons and inelastic tunneling electrons.

5.2 Elastic Tunneling Through QDs Arrays

The electron Hamiltonian for elastic resonant tunneling is give by[8]

$$H = \sum_{ik} \varepsilon_{ik} c_{ik}^{\dagger} c_{ik} + \sum_{k} \left(\varepsilon_{k_L} c_{k_L}^{\dagger} c_{k_L} + \varepsilon_{k_R} c_{k_R}^{\dagger} c_{k_R} \right) + \sum_{k} \left[V_{ikL} \left(c_{kL}^{\dagger} c_{ik} + c_{ik}^{\dagger} c_{kL} \right) + V_{ikR} \left(c_{kR}^{\dagger} c_{ik} + c_{ik}^{\dagger} c_{kR} \right) \right]$$

where,

1. ε_{ik} is $i-th$ miniband energy of $i-th$ resonant state in double barrier quantum dot arrays.

2. c_{ik}, c_{kL} and c_{kR} are creation operators of electrons in the quantum well i^{th} resonant state with $i-th$ miniband energy ε_{ik} for left and right electrode

3. $c_{ik}^{\dagger}$, $c_{kL}^{\dagger}$ and $c_{kR}^{\dagger}$ are annihilation operators of electrons in the quantum well i^{th} resonant state with $i-th$ miniband energy ε_{ik} for left and right electrode

4. V_{ikL} and $V_{ikR}$are the matrix element of elastic tunneling from left and right electrodes to the $i-th$ miniband state in the quantum well respectively.

It is assumed that the coupling of electrons in metals to quantum well energy level is by elastic process only. The elastic hopping matrix elements $V_{k_{Al(Pb)}}$determines the elastic coupling of the electrons in the aluminum and lead to electrons in quantum dot energy level $\varepsilon_{k_{Al(Pb)}}$. The coupling of metals to quantum well $\Gamma_{Al(Pb)}$ can be determined by these matrix elements using the following formula:

$$\Gamma_{Al} = 2\pi |V_{Al}|^2 \rho_{Al}$$

on tunneling spectroscopy at room temperature to resolve vibrational energy level of molecules, thermal energy distribution of electrons should be less than $\triangle E \sim 6.63mV$. The designed quantum dots electron energy filters can only narrow down thermal distribution of electron down to only $\triangle E_{2dQDs} \sim 10mV$. Hence, even though quantum dot electron energy filters can narrow down thermal distribution of electrons from $\sim 25mV$ down to $\sim 10mV$, its not enough to perform high resolution inelastic electron tunneling spectroscopy at room temperature. Also, quantum dot energy filters suffer from charge trapping, which degrades there performance with repeated current-voltage measurement.

$$\Gamma_{Pb} = 2\pi |V_{Pb}|^2 \rho_{Pb}$$

where, $\rho_{Al} = \sum_k \delta\left(\varepsilon - \varepsilon_{k_{Al}}\right)$ and $\rho_{Pb} = \sum_k \delta\left(\varepsilon - \varepsilon_{k_{Pb}}\right)$are the densities of states in aluminum and lead respectively. Since the bandwidth miniband in quantum well is much smaller than the bandwidth of energy level in aluminum and lead, one can approximate that the density of states ρ_{Al} and ρ_{Pb} are constant at in resonant region.

5.3 Inelastic Tunneling Through QDs Array

For the electrons localized in quantum dots well, electron-phonon interaction Hamiltonian is given by[9]

$$H_{int} = \sum_q M_q \left(a_q + a_q^\dagger\right) \sum_k c_{k+q}^\dagger c_k$$

where $a_q$and $a_q^\dagger$ are phonon creation and annihilation operators respectively.

Assuming Einstein phonon with energy $\hbar\omega_0$ at low temperature, we can write electron-phonon coupling constant g as:

$$g = \sum \frac{|M_q|^2}{(\hbar\omega_0)^2}$$

5.4 Current Density Through QDs Array

The Landauer-Buttiker (LB) method establishes the fundamental relation between the wave functions (scattering amplitudes) of a non interacting quantum system and its conducting properties. Here I used Landauer-Buttiker formalism to calculate the tunneling current through QDs array sandwiched between two metal contacts. The current from the left to the right is determined by the distribution function only of the left contact:

$$J_{Al\to Pb} = e\sum_{\lambda}\int_0^{\infty} T_{Al\to Pb}(k_l)\, v_{l_{Al}}(k_l)\, f_{Al}(k_l,\lambda)\,\frac{dk_l}{2\pi}$$

where k_l is longitudinal momentum and $v_{l_{Al}}(k_l)$is the velocity of the electron in aluminum with momentum k_l. We know,

$$v_l = \frac{\partial E_l(k_l)}{\hbar\partial k_l}$$

Using the above expression. We get

$$J_{Al\to Pb} = \frac{e}{h}\sum_{\lambda}\int_{U_{Al}}^{\infty} T_{Al\to Pb}(E_l)\, f_{Al}(E_l,\lambda)\, dE_l$$

where U_{Al} is bottom of conduction band in aluminum. Similar expression for the current from the right to the left is given by

$$J_{Pb\to Al} = \frac{e}{h}\sum_{\lambda}\int_{U_{Pb}}^{\infty} T_{Pb\to Al}(E_l)\, f_{Pb}(E_l,\lambda)\, dE_l$$

The final expression for current density at a voltage bias V is give by

$$J(V) = \frac{e}{h}\int_{-\infty}^{\infty} T(E)\left[F_{Al}(E) - F_{Pb}(E)\right]dE$$

Where F_{Al} and F_{Pb} is Fermi energy distribution of electrons in aluminum and lead respectively. And the transmission probability $T(E)$ for QDs array.

When a bias is applied across the barrier, the voltage drop is equally distributed between the two barriers. Taking into account the energy shift in a Fermi distribution function due to bias voltage, one obtains:

$$J(V) = \frac{e}{h}\int_{-\infty}^{\infty} T(E)\left[F_{Al}(E+eV) - F_{Pb}(E)\right]dE$$

For a 3D tunneling system, above equation can be written as[9]:

$$J(V) = \frac{e}{h}\int_{0}^{\infty} T(k).dk_l \int d^2k_t v_l \left[f_{Al}(\varepsilon_k) - f_{Pb}(\varepsilon_k)\right]$$

Since at lower energies $T(E) = 0$, Integration over E should be actually performed from the maximum of two conduction band bottoms.

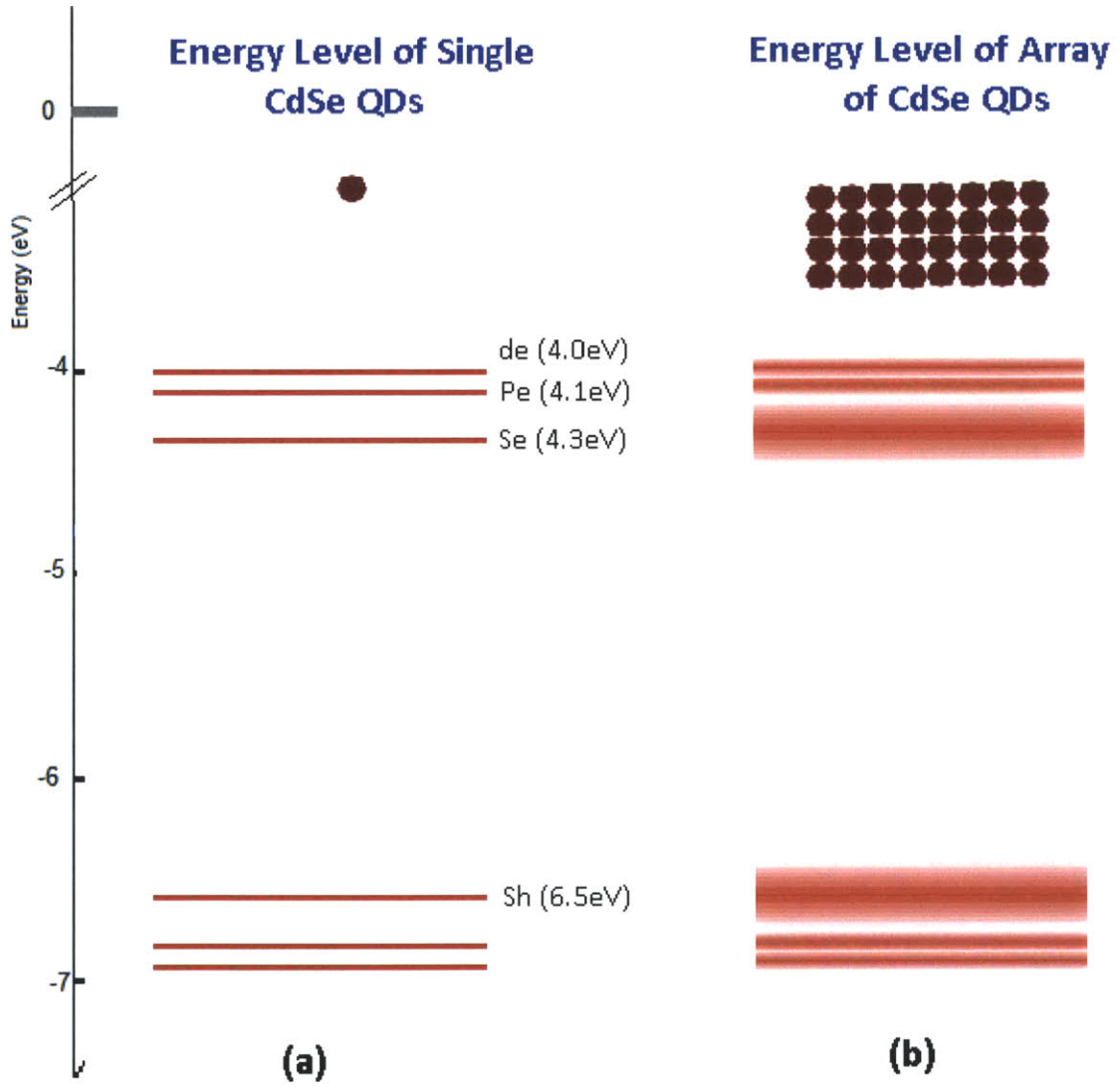

Figure 5.1: Energy Level Diagrams of (a) Single *CdSe* QD and (b) formation of energy minibands in 2-dimentianal array of *CdSe* QDs

Chapter 6

Fabrication of CdSe QDs Electron Energy Filters

6.1 Introduction

As described earlier, the reason of the thermal broadening of IETS peak is due to thermal distribution of electrons in metal. The discrete energy levels in quantum dots can be used to narrow down the thermal distribution of electrons. This chapter describes the fabrication of electron energy filter using $CdSe$ quantum dots. The device consist of $ITO - Al_2O_3 - QDs - Ag$ structure as shown in Figure6.1 .

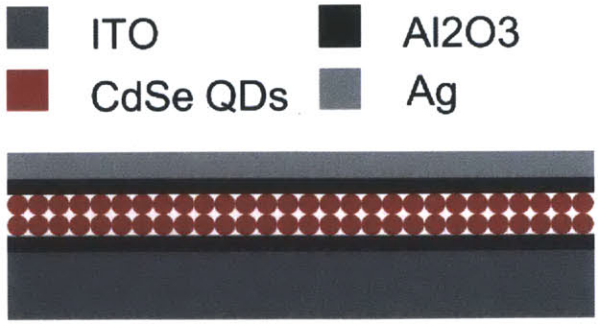

Figure 6.1: Schematic Diagram of device structure of ITO-QDs-Ag Devices

To understand how this quantum dot energy filters works, one has to consider the band-diagram

of this device. The band-diagram of $ITO - Al_2O_3 - QDs - Ag$ device is shown in Figure 6.2. At a particular bias voltage, when Fermi level of ITO aligns with LUMO (lowest unoccupied

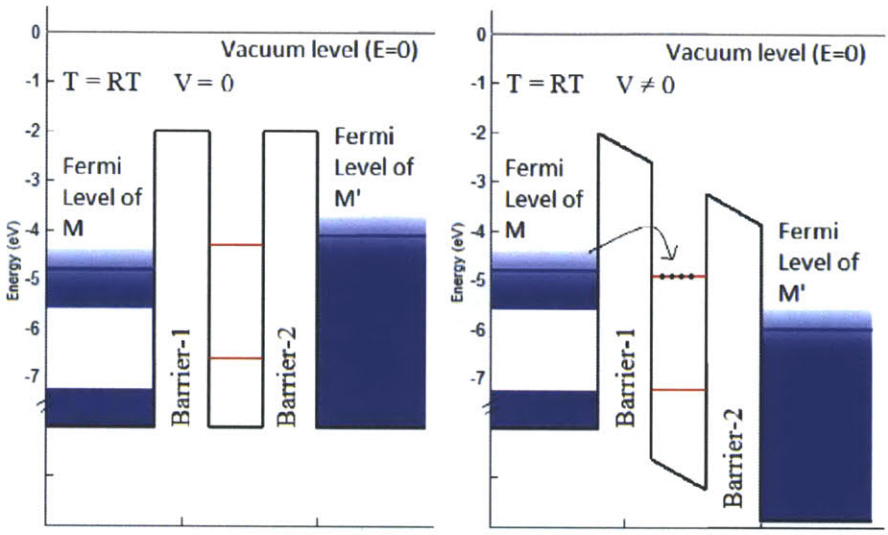

Figure 6.2: Band diagram of M-I-QD-I-M Devices

molecular orbital) of $CdSe$ quantum dots, large number of electrons can tunnel through barrier-1 contribution to large tunneling current. The electrons tunneling through barrier-1 can only occupy discrete energy levels available in $CdSe$ quantum dots. Hence, these electrons, when tunneling from quantum dots to Ag through barrier-2 will have narrow distribution of energies equal to energy states of $CdSe$ quantum dots.

6.2 Fabrication and of ITO-QDs-Ag Devices

These devices are fabricated on pre-cleaned indium tin oxide (ITO) coated glass substrate. First, $5nm$ thick Al_2O_3 is deposited on ITO substrate using e-beam evaporator system. Then $CdSe$ quantum dots dispersed in toluene are spin coated on $ITO - Al_2O_3$ substrate at $3000rpm$ for $60s$. SEM image of spin coated CdSe quantum dots on ITO substrate is shown in figure 6.3. Silver paste is used as top metal electrode. Final device structure consisted of $ITO - Al_2O_2 - CdSeQDs - Ag$ layers.

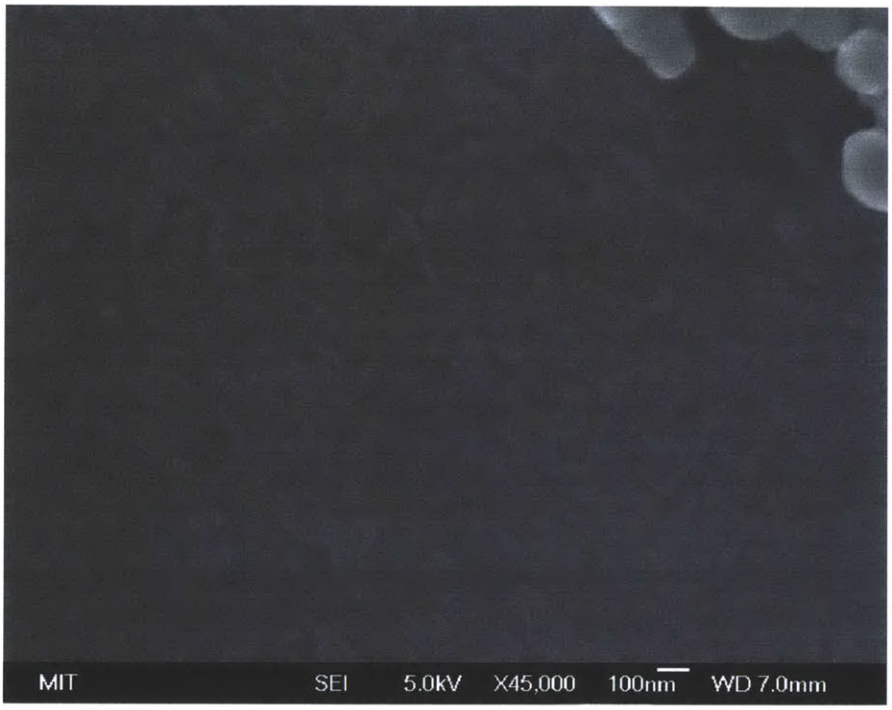

Figure 6.3: Scanning electron microscope image of CdSe quantum dots spin coated on ITO substrate

6.3 Current-Voltage Characteristics of $ITO - Al_2O_2 - CdSeQDs - Ag$ Devices

For making top electrical contacts, silver paste is used. One contact is made at the protected region of ITO and other contacts is made on top of top spin coated $CdSe$ layer as schematically shown in figure 6.4 .

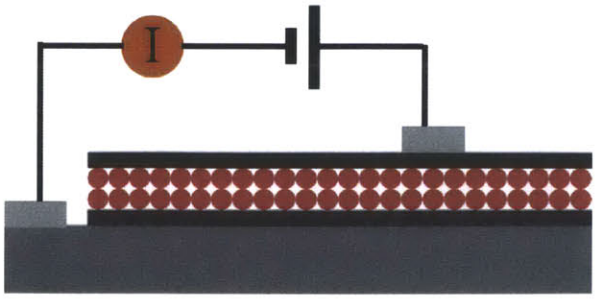

Figure 6.4: Schematic representation of electrical connection made on $ITO - Al_2O_3 - CdSeQDs - Ag$ Devices

Current-Voltage characteristics is measured using HP 4156A semiconductor parameter analyzer. Positive bias is applied to Ag electrodes and negative bias is applied to ITO. Figure 6.5 shows the current-voltage characteristics of three different $ITO - Al_2O_3 - CdSeQDs - Ag$ devices.

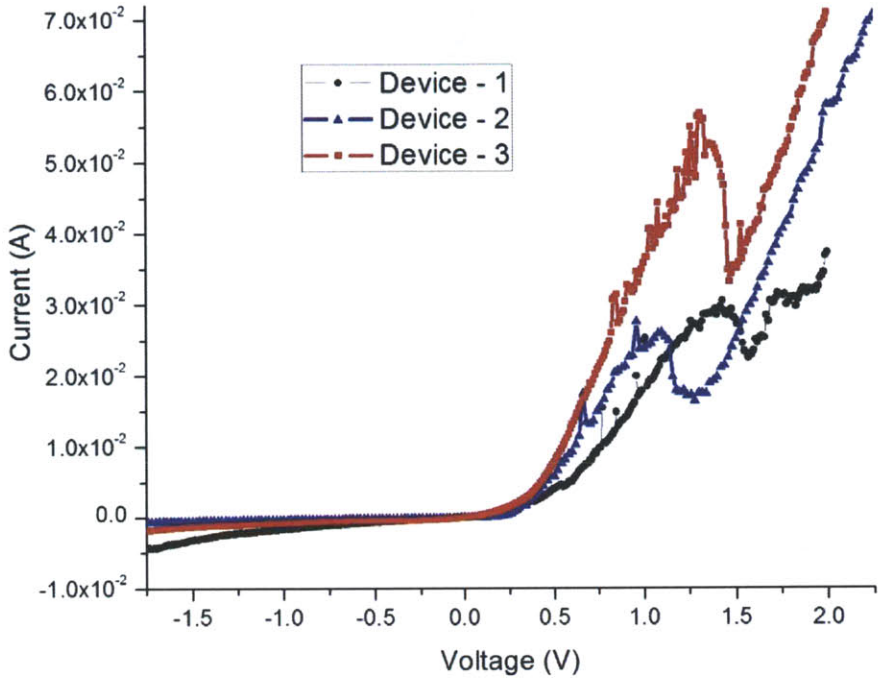

Figure 6.5: Current-Voltage Characteristics of three different $ITO - QDs - Ag$ Devices

Since electrical contacts are made using silver paste, fine control over the devices cross section is not possible. This variation in the device cross-section led to slight variation in current-voltage characteristics of three devices shown in figure 6.5. There are two important characteristics of the current-voltage measurement observed in these devices.

First, overall a "Schottky diode" characteristics is observed i.e. there is no or very low current observed in reverse bias condition. To explain this observation, lets consider band diagram at $CdSeQDs - Ag$ interface. The work function of Ag is $4.8eV$ [16]. Though the electron affinity of $CdSe$ quantum dots relative to vacuum has not previously been measured, the theoretically predicted electron affinity is likely near $4.3eV$ [17] (or slightly less than $4.3eV$ as electron affinity deceases with decreasing the size of quantum dots). Figure 6.6(A) shows the band diagram of Ag and $CdSe$ QDs when Ag and $CdSeQDs$ are far apart. When they are allowed to make contacts,

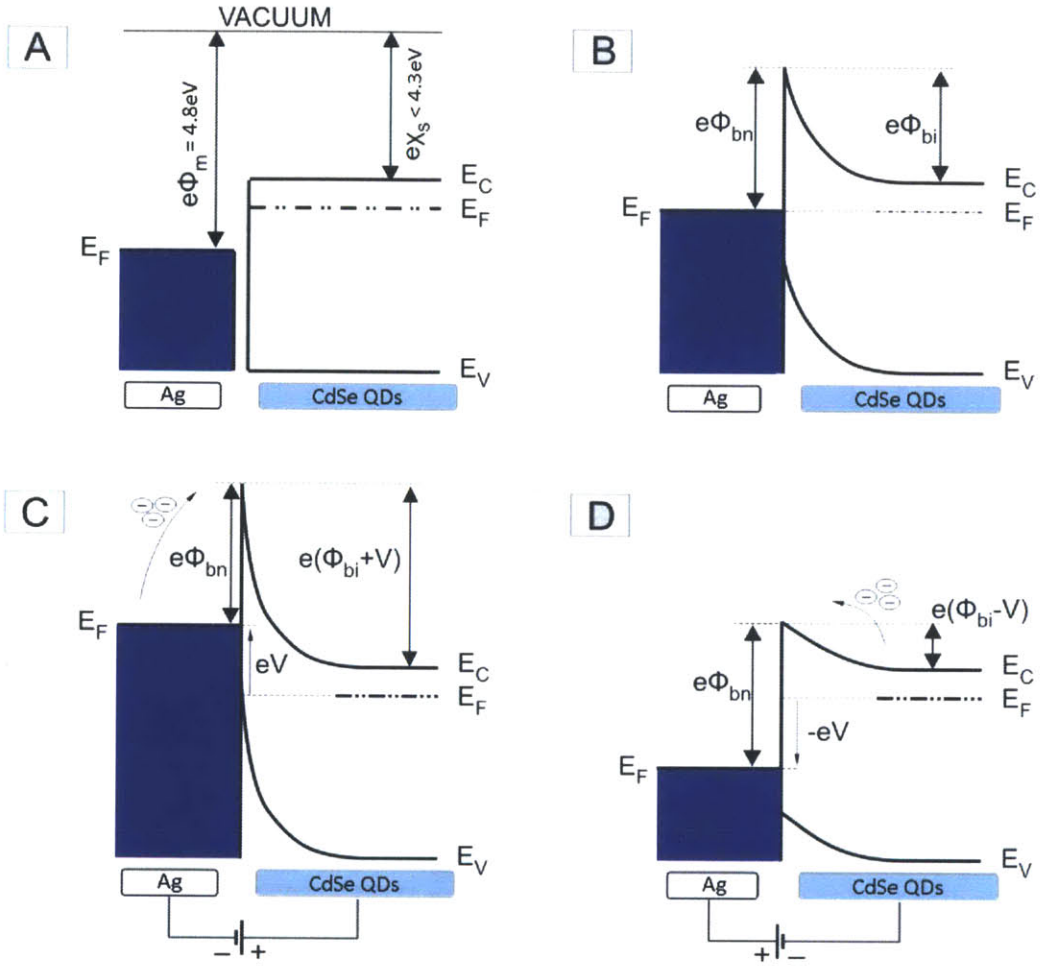

Figure 6.6: Band Diagram of $Ag - CdSeQDs$ Interface and formation of Schottky barrier

since the work function of the Ag is appreciably larger than the electron affinity of $CdSe$ quantum dots, a Schottky barrier ϕ_{bn} is created at the interface (figure 6.6(B)). This Schottky barrier is seen by electrons in metal and is equal to $\phi_{bn} = \phi_m - \chi_s$ where ϕ_m is Fermi level of Ag and χ_s is electron affinity of $CdSe$quantum dots. On quantum dots side, ϕ_{bi} is potential barrier seen by electrons in the conduction band trying to move into the metal.

When a reverse bias is applied (i.e. negative bias to Ag) as shown in figure 6.6(C), the electron in metal sees ϕ_{bn} and hence does not contribute to current. This is why the current in reverse bias is small. On the other hand in forward bias condition (i.e positive bias to Ag) the potential seen by electrons in conduction band of quantum dots reduces to $\phi_{bi} - V$ where V is applied bias (Figure 6.6(D)). At certain threshold voltage V_{th} the potential barrier ϕ_{bi} reduces to zero and electrons can

contribute to current. For $ITO - Al_2O_3 - CdSeQDs - Ag$ devices the value of threshold voltage is found to be $V_{th} \sim 0.25V$.

Another interesting characteristics of current-voltage measurement is observation of negative differential resistance. To understand this interesting behavior, lets consider the band diagram of $ITO - QDs$ interface as shown in figure 6.7. The work-function of Indium tin oxide (ITO) is

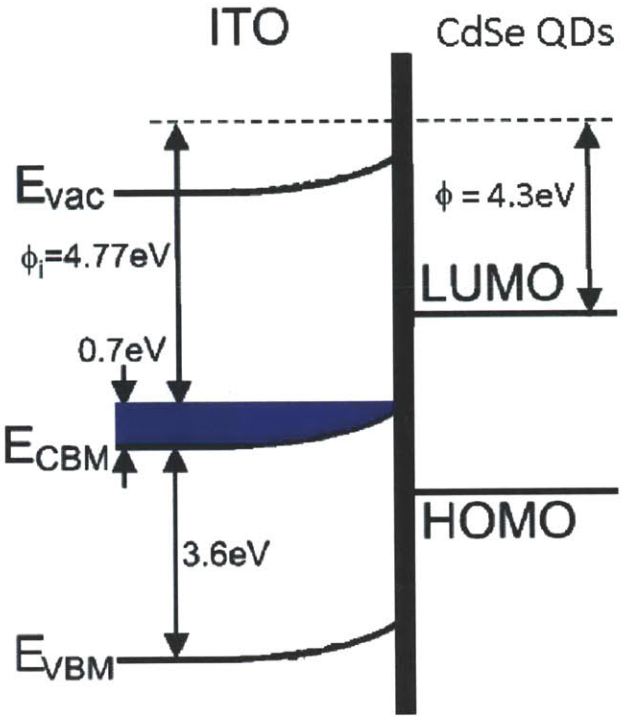

Figure 6.7: Band diagram of ITO-QDs interface

$4.77eV$ [14, 15]. However, there is an important difference between ITO and a metal electrode: ITO consists of Sn-doped (n-doped) In_2O_3, an intrinsic insulator. Even as an n-doped conductor, ITO still has a wide band gap from$3.50eV$ to $4.06eV$ [12, 13]. Based on how ITO is grown (% of O_2 in growth environment) the Fermi level is either in conduction band or slightly above ($\sim 0.7eV$) the conduction band [18][14].

The observation of negative differential resistance in current-voltage characteristics of $ITO - Al_2O_3(5nm) - CdSeQDs(\ 80nm) - Ag$ can be explained using the theoretical model developed

for arrays of quantum dots sandwiched between two metal electrodes. As described in chapter 5, $2D$ array of quantum dots can be modeled as resonant tunneling diode with several minibands having finite mini-bandwidth. Figure 6.8 shows the simplified band diagram of $ITO - Al_2O_3 -$

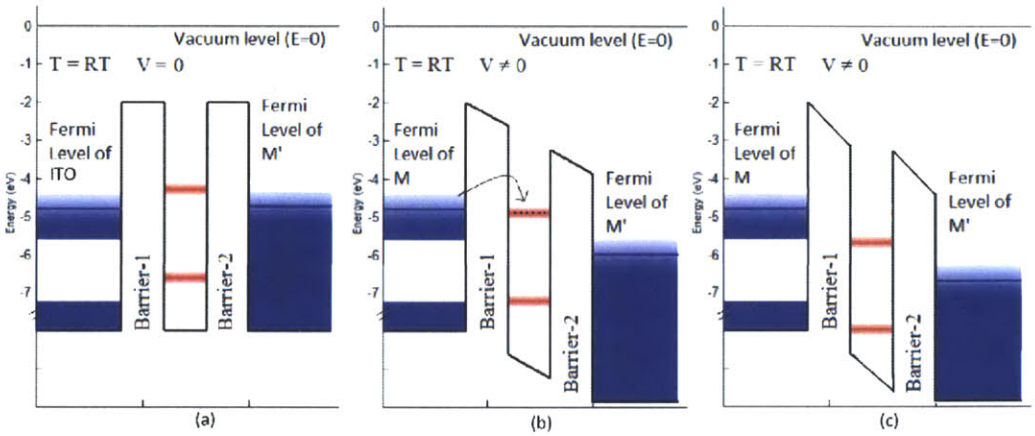

Figure 6.8: Band diagram of the$ITO - Al_2O_3(5nm) - CdSeQDs(\ 80nm) - Al_2O_3(5nm) - Ag$ Devices

$CdSeQDs - Ag$ devices modeled as double barrier resonant tunneling diode. Initially at low bias condition, when Fermi level of ITO is below the first energy state of $CdSe$ quantum dots, no electron tunneling is possible as there is no energy state available to be occupied by tunneling electron. Since there is no electron tunneling, very low current is observed at this bias voltage. As the bias voltage is gradually increased, at around $\sim 0.25V$, Fermi level of ITO aligns with the first energy miniband of $CdSeQDs$ as shown in figure 6.8(b). At this bias, large electrons can tunnel and occupy the energy state of quantum dots resulting in sudden increase in current (figure 6.5). When the bias voltage is further increased, the first energy state of quantum dots now aligns with the bandgap of ITO.As there are now electron available in the bandgap of ITO to contribute to tunneling current, the total current will again decrease (figure 6.5). This led to observation of negative differential resistance in $ITO - Al_2O_3 - CdSeQDs - Ag$ devices.

The peak-width of peak observed in IV measurement is $\sim 1V$, as shown in figure 6.8, this peak is observed due to electron tunneling from conduction band in ITO to miniband of array of quantum dot structure. The width of conduction band in ITO is $\sim 0.7mV$ [18][14] and varies with % of oxygen present in ITO. Given that width of conduction band in ITO is not precisely known,

its difficult to predict the width of minibands formed in $CdSe$ quantum dots array.

These devices have some technological limitation in terms of device fabrication. These limitations are as follows -

1. For tunneling barrier, Al_2O_3 layer is deposited using e-beam evaporator. Such deposited thin film usually have some pin holes and can contribute to leakage current which is much higher than tunneling current.

2. Since the top electrical contacts are made using Ag conducting paste, there is a difficulty in keeping the same device cross-section all across the various fabricated devices.

3. The band diagram of ITO is not precisely known, hence the width of minibands in 2-dimentional array of quantum dots can not be derived from IV characteristics of these devices.

To overcome these problems, new sets of devices are fabricated were aluminum is used as one electrode. On top of aluminum an oxide layer is grown using Rf oxygen plasma oxidation technique. The grown aluminum oxide acts as tunneling barrier. For top electrode Pb is used. The final device structure consist of $Al - Al_2O_3 - QDs - Pb$ system. Fabrication of these devices are discussed in next section.

6.4 Fabrication of $Al - Al_2O_3 - QDs - Pb$ Tunneling Device

The device fabrication process consist of following steps

1. $1mm$ wide, $10mm$ long and $100nm$ thick aluminum electrode is deposited on pre-cleaned glass substrate using thermal vapor deposition system.

2. Aluminum oxide is grown on top of Al using Rf plasma oxidation process. Oxide growth is carried out for $10s$ at Rf power of $10W$ and oxygen flow rate of $1sccm$.

3. $480nm$ CdSe quantum dots dispersed in toluene are spin coated on top of aluminum oxide at $3000rpm$ for $60s$. For comparison purpose another device is fabricated without quantum dots.

4. For top metal electrode various metals such as Ag, Au, Al and Pb are deposited using thermal vapor deposition system.

Table 6.1 tabulates resistance and capacitance of some $Al - Al_2O_3 - QDs - M'$ devices, where,

Device Structure	Resistance	Capacitance
Al-Al2O3-Pb	0.8K	34nF
Al-Al2O3-QDs-Pb	~7M	4.5nF
Al-Al2O3-QDs-Au	~10	-
Al-QDs (480nm)-Al, 3000rpm	~3M	4nF
Al-Al2O3-QDs-Ag	~4	-

Table 6.1: Resistance and Capacitance of $M - I - QDs - M$ Devices

M' is Pb, Au, Ag, and Al. It can be seen in table 6.1 that the resistance of devices with Au and Ag as top electrode is very small. This is due to the fact that these metals have small atomic size and high kinetic energy at room temperature. During the thermal vapor deposition of these metals, they tend to diffuse through the QDs layer resulting in very small device resistance. On the other hand Pb has large atomic size and low kinetic energy at room temperature and hence can not diffuse through $CdSe$ QDs layer. For this reason final current-voltage measurement is performed on $Al - AL_2O_3 - CdSeQDs - Pb$ devices.

6.5 Current-Voltage Characteristics of $Al - Al_2O_3 - QDs - Pb$ Devices

Indium soldering is used to make electrical contact with Al and Pb leads. Current-voltage measurement is performed using Keithley 6487 picoammeter/voltage source. The common observation of $Al - Al_2O_3 - QDs - Pb$ devices is that they have very high resistance. Also, the resistance

of devices increases after every run of current-voltage measurement indicating charge trapping in surface states of $CdSe$ quantum dots. Figure 6.9 shows the current-voltage characteristics of

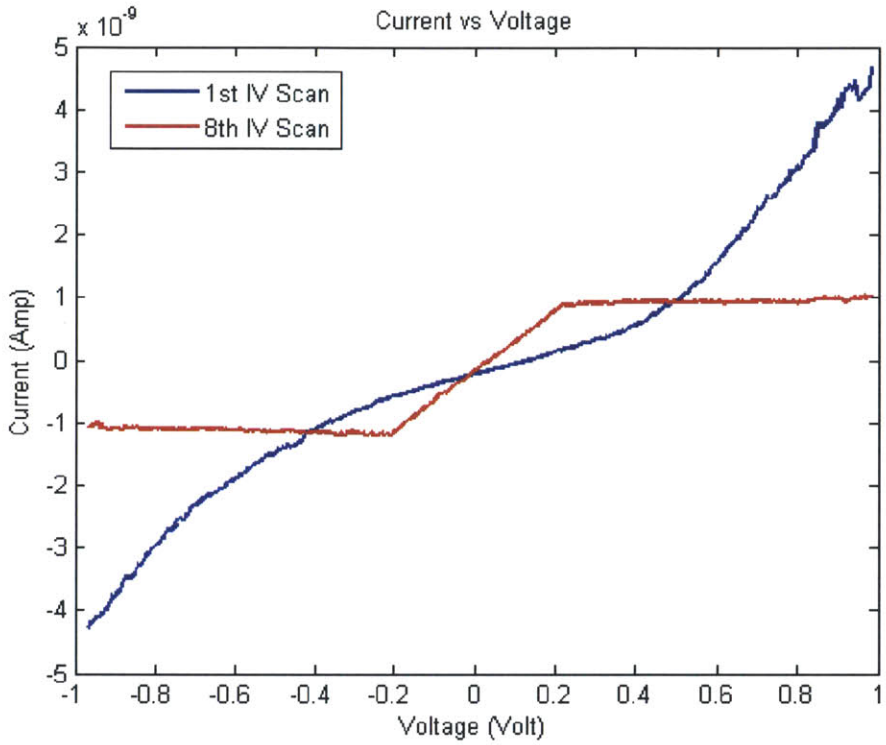

Figure 6.9: Current-Voltage Characteristics of$Al - Al_2O_3 - QDs - Pb$ Devices

$Al - Al_2O_3 - QDs - Pb$ device for $1st$ and $8th$ run. The IV curve tends to move towards $x - axis$ i.e current tends to decrease until the current reaches the limit of minimum current our system can measure.

This observation can be explained by considering charge trapping in quantum dots surface energy states. When the current-voltage characteristics is measured for the first time, tunneling electron will occupy certain surface energy level of $CdSe$ quantum dots. Now, if the electrons have long lifetime, they will retain their position in these energy levels. When current-voltage measurement is repeated again, these electrons in surface states of the quantum dots will inhibit further tunneling of electrons from Al to Pb thereby decreasing tunneling current. Such memory effect of electron trapping in quantum dots surface states is also been observed by other authors[19].

This observation of charge trapping can further be tested by performing current-voltage char-

acteristics at low temperature. First, device is cooled to $4.2K$ and current-voltage measurement is performed. The device showed very high resistance with virtually no tunneling current ($< 10^{-12}A$). This can be explained by the fact that all the electrons are in valance band and hence will not contribute to any tunneling current. The device is then brought back to room temperature and a current-voltage measurement is performed.

Figure 6.10 shows current-voltage measurement of device which was cooled to $4.2K$ and then

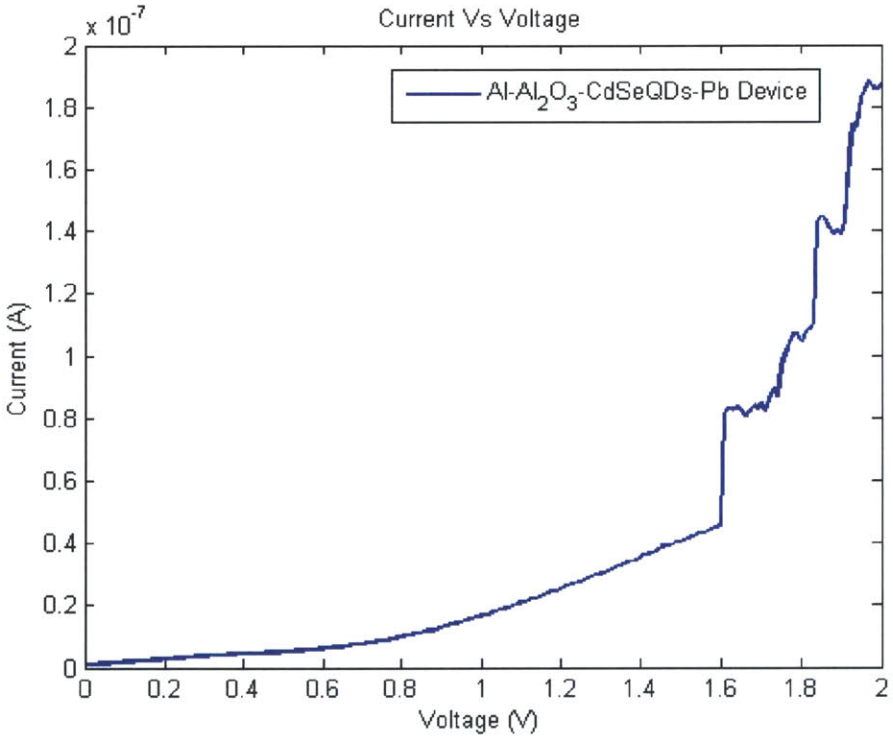

Figure 6.10: Current-Voltage characteristics of $Al - Al_2O_3 - QDs - Pb$ devices which were cooled to $4.2K$ and then brought to room temperature for measurement

brought back to room temperature for current-voltage measurement. Positive bias is applied to Pb electrode and voltage is swept from $-2V$ to $2V$ in steps of $10mV$. The zero current gap in the current-voltage characteristics can be associated with the band gap of $CdSe$ quantum dots. Current onset for bias occurs when there is resonance between the Fermi energy of Al and the first quantized conduction energy level of $CdSe$ quantum dots. This led to stairs like characteristics in current-voltage measurement as shown in figure 6.10.

In order to clearly observe the position of these current steps, first derivative of current is numerically calculated and plotted in figure 6.11 . The position of the first, second and third peaks

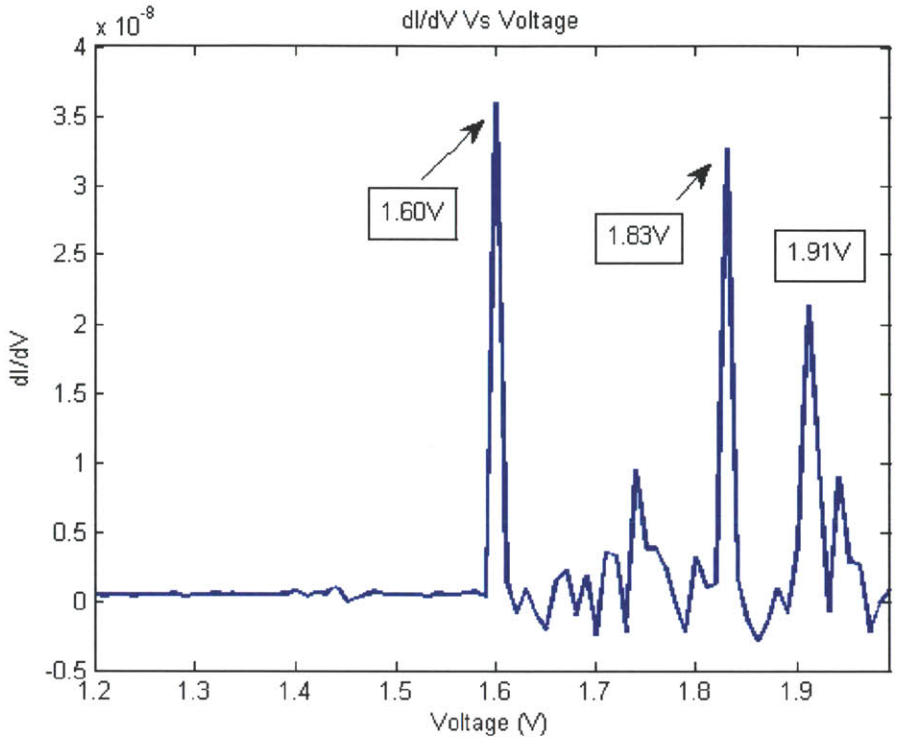

Figure 6.11: $\frac{dI}{dV}$ vs voltage measurement of $Al - Al_2O_3 - QDs - Pb$ devices which were cooled to $4.2K$ and then brought to room temperature for measurement

are at $1.6V$, $1.8V$ and $1.91V$ respectively. Distance between the first doublet peaks is $0.23V$ which matches with the value reported in reference [22][21]. The FWHM of first peak in figure 6.11 is around $\sim 10mV$ suggesting that the bandwidth of miniband in 2-dimentional array of quantum dots is $\triangle E_{2dQDs} \sim 10mV$.

This stairs like feature seems to disappear on second run of current-voltage measurement. This observation is due to electron trapping in surface energy states of CdSe quantum dots which reduces further tunneling probability. For comparison figure 6.12 shows the current-voltage at low temperature, first run after bringing the sample back to room temperature and the second run. During all the measurement the sample is kept in dark.

The conclusion of this chapter is that $CdSe$ quantum dots can be used for electron energy

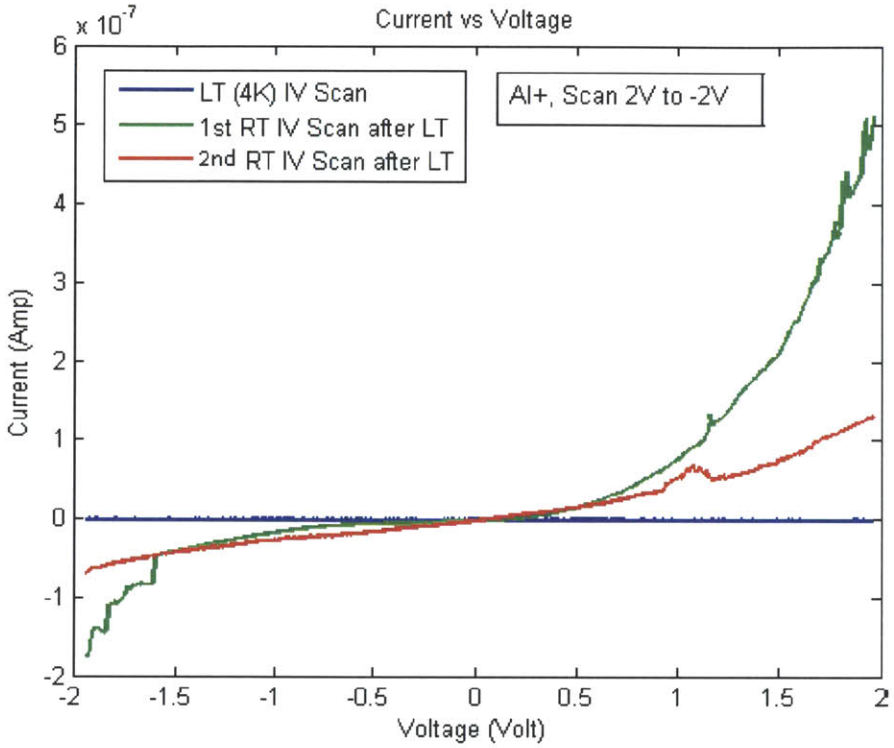

Figure 6.12: Current-Voltage Characteristics of$Al - Al_2O_3 - QDs - Pb$ Devices for Temperature Cycle

filtering. However, there are two reasons which limits the use of these quantum dots as energy filter for application in inelastic electron tunneling spectroscopy. These two limitations are as follows

1. Although individual $CdSe$ quantum dots have very fine discrete energy levels, the $2D$ array of quantum dots used in above devices from minibands with finite bandwidth. This bandwidth is estimated to be around $\sim 10meV$. On the other hand as we discussed in chapter 4, required filtering of electron energy to perform room temperature inelastic electron tunneling spectroscopy is $\sim 6.6meV$.

2. Other major limitation of using quantum dots for electron energy filtering is electron trapping in surface energy state of quantum dots. These trapped electrons inhibit further tunneling of electrons resulting in very low current. Such low current is not suitable to perform inelastic electron tunneling spectroscopy.

To avoid formation of minibands in array of quantum dots, electron transport through single quantum dot is studied.

Chapter 7

Electron Transport through Single *CdSe* Quantum dot

The device structure discussed in chapter 6, consisted of an array of quantum dots sandwiched between two metals. In an array of quantum dots, each energy level of quantum dots appear as miniband which limits the resolution with which electron energy filtering is achievable in such system. This chapter studies electron transport through single quantum dot. In current system, it is expected that the current will be observed only through individual energy level of quantum dots as compared to minibands formed in an array of quantum dots. Current-Sensing atomic force spectroscopy (CSAFM) is used to study electron transport through single quantum dot. This chapter first describes current-sensing atomic force microscopy, followed by current-voltage spectroscopy of single quantum dot and conclude with presenting measured data.

7.1 Current-Sensing Atomic Force Spectroscopy

In current sensing AFM (CS-AFM) an ultra-sharp AFM cantilever, coated with conducting film, probes the conductivity and topography of the sample surface. A bias voltage is applied to the sample while the cantilever is kept at virtual ground. The cantilever probe is connected to a current pre-amp which converts the measured current into voltage [20]. This voltage is then fed into data

acquisition system and used to calculated current. As in contact mode, the tip force is held constant throughout the scan. Current is used to construct the conductivity image. It is also used for current-voltage spectroscopy where the cantilever tip is kept at a fixed location and bias voltage is sweep and current is measured.

7.2 AFM Imaging of *CdSe* Quantum Dots

CdSe quantum dots dispersed in toluene are spin-coated on *ITO* coated glass substrate at $3000rpm$ for $45s$. The sample is allowed to dry for few hours before SPM imaging. For atomic force microscope imaging, contact mode is used. AFM tip is brought into gentle contact with the sample and then scanned in raster fashion across the sample surface. The system was set to maintain the tip at a constant height, for high resolution imaging of very flat surfaces. In constant height mode, the feedback loop no longer adjust the tip force. This lack of feedback reduces signal noise, enabling atomic-level resolution imaging of very flat samples. Figure 7.1 shows the atomic force microscope image of *CdSe* quantum dots.

7.3 Current-Voltage Spectroscopy of Single CdSe Quantum Dot

First, an AFM image is taken and quantum dot location is identified. The tip is than moved over a selected quantum dot as shown in figure 7.2 for current-voltage spectroscopy. This system is schematically shown in figure 7.3.

For current-voltage spectroscopy, tip is kept at virtual ground and the bias is applied to indium tin oxide. Voltage bias is swept from $-200mV$ to $200mV$ in steps of $10mV$ and range for current sensing is set to $10nA$. An ultra low bias current pre-amp is used to convert the tunneling current into voltage. Figure 7.4 shows the circuit diagram of the current pre-amplifier used for current-voltage spectroscopy system. The voltage from pre-amp was measured using Agilent 34401A multimeter. A matlab code was written for data acquisition and plotting.

The difference between current device geometry and the device discussed in chapter 6 is that

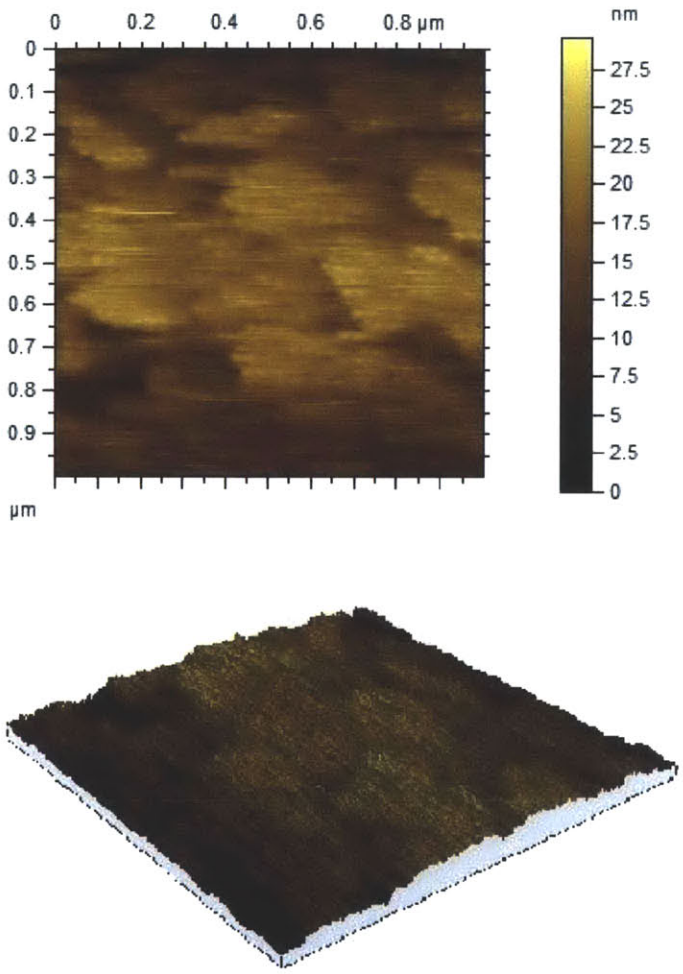

Figure 7.1: AFM image of CdSe Quantum dots spin coated on gold coated mica substrate

, in current system electron transport is through single quantum dots leading to observation of individual energy levels. On the other hand, for devices discussed in chapter 6 current transport was through array of quantum dots which is equivalent to double barrier junction with minibands. The electron transport through such system leads to resonant tunneling.

7.4 Result and Discussion

Current-voltage measurement of a single CdSe quantum dot is shown in figure 7.5 . The flat lines observed at $10nA$ is due to the saturation of the current pre-amplifier. As it can be seen in

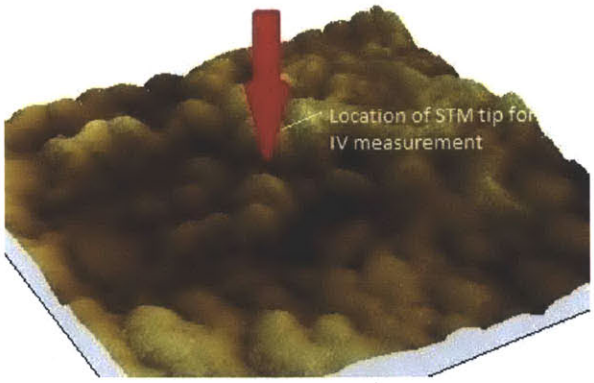

Figure 7.2: STM tip over a quantum dot for Current-Voltage Spectroscopy

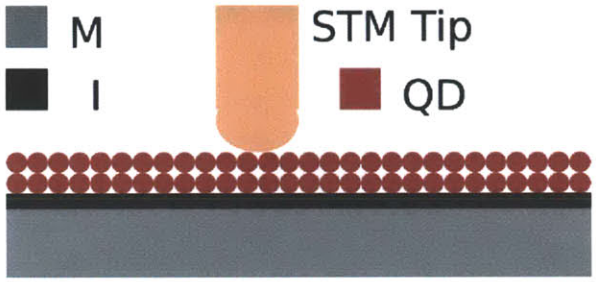

Figure 7.3: Schematic diagram of Current-Voltage Spectroscopy of individual QDs

figure 7.5, a resonant peak is observed in current-voltage measurement, this peak is similar to the peak observed in $ITO - Al_2O_2 - CdSeQDs - Ag$ devices (figure 6.5) for "array of quantum dots system". This peak is observed reproducibly in different quantum dots but disappear if the current-voltage measurement is performed on same quantum dot twice. The observation can be explained on basis of charge trapping in the surface states of quantum dots. Such observation of charge trapping in quantum dots leading to change in current-voltage measurement is also observed in $Al - Al_2O_3 - QDs(Array) - Pb$ devices (figure 6.9).

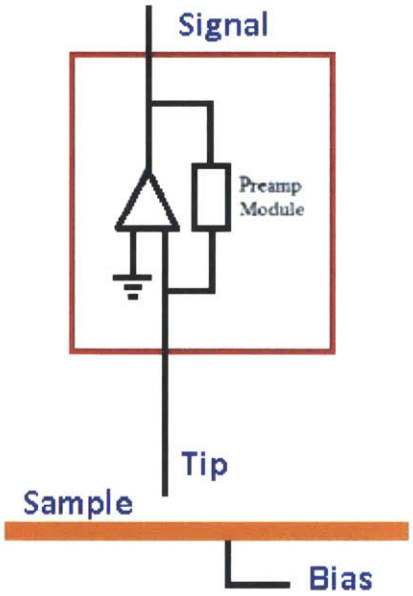

Figure 7.4: Circuit Diagram of current pre-amp used in IV Spectroscopy system

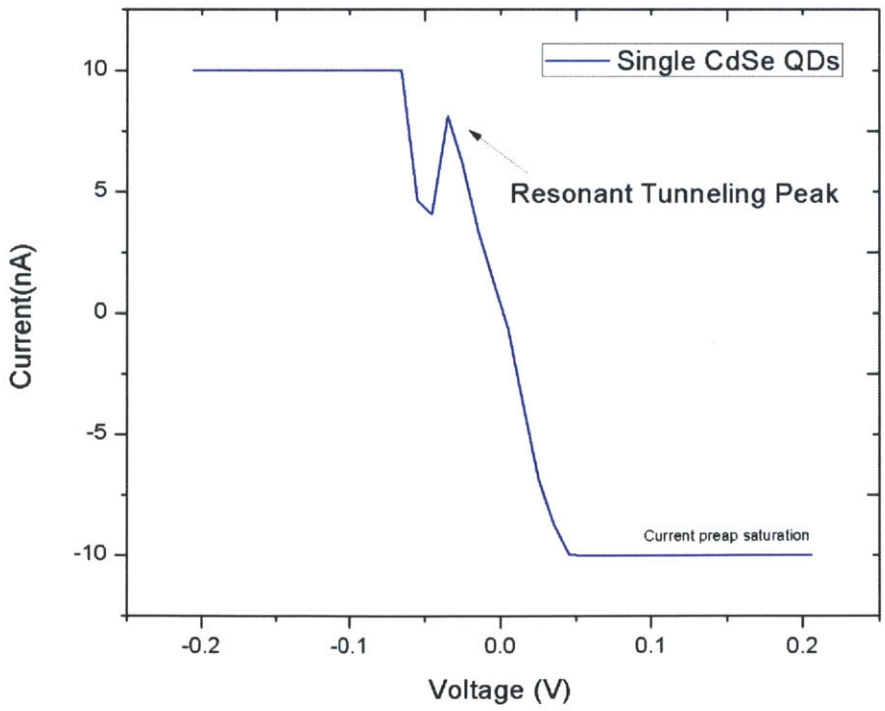

Figure 7.5: Current-Voltage Spectroscopy of individual CdSe QDs using CSAFM

Chapter 8

Summary and Conclusion

8.1 Summary

To summarize, we started with a problem of performing high resolution inelastic electron tunneling spectroscopy to resolve molecular vibrations at room temperature. At room temperature, electrons possess thermal energy kT ($\sim 25mV$) and occupy broad range of energy levels available in metals. This thermal distribution of electrons around Fermi-level limits the resolution of inelastic electron tunneling spectroscopy.

I proposed to use "electron energy filters" to narrow down thermal distribution of electrons in order to increase the resolution of inelastic electron tunneling spectroscopy at room temperature. Before designing such "electron energy filters", one has to quantitatively determine the specification i.e. extent of filtering (or Q-factor) required to perform room temperature inelastic electron tunneling spectroscopy. This information is derived by studying thermal broadening on IETS peaks w.r.t temperature. Inelastic tunneling spectra is measured at various temperature to determine maximum temperature at which IETS peaks can be resolved. This information is used to derive the "maximum energy distribution" $\triangle E$, of electrons which can still give usable IET spectra that can clearly resolve vibrational modes of molecules.

For $HCOOH$, vibrational energy modes are separated by approximately $\sim 50mV$ energy. Now,

in order to resolve $HCOOH$ energy levels, peak widths in IET spectra should not be more than $\sim 50mV$. By studying the variation of IET spectra peak-width w.r.t temperature, we know that this corresponds to a temperature $T_{max} \sim 77K$ (section 4.4). At this temperature, electrons have thermal energy distribution of $\triangle E \sim 6.63mV$. Hence, in order to resolve $HCOOH$ peaks at room temperature, one has to design electron energy filter that can narrow down thermal distribution of electrons from $\triangle E \sim 25mV$ down to $\triangle E \sim 6.63mV$. It must be noted that, this requirements will change with molecules under study. For example, if for a molecule, the difference between individual vibrational energy level is of the order of $\sim 20mV$ than T_{max} will be around $\sim 10K$ and allowed distribution of energy level will be only $\triangle E \sim 0.8meV$.

For designing electron energy filter, I used quantum dots. We know that number of electron in an energy state E is give by $n(E) = \rho(E)f(E)$. Where, $\rho(E)$ is energy density of state and $f(E)$ is Fermi function. Now, for metals $\rho(E)$ is a continuous function so every electrons possessing some thermal energy can occupy available energy states resulting in thermal distribution of electrons. On the other hand, quantum dots due to there small size have discrete values for density of states i.e. $\rho_{QD}(E)$ is like a delta-function. So even though electrons have broad distribution of thermal energy at room temperature, they can only occupy certain fixed energy levels available in quantum dots. In other words, we can narrow down thermal energy distribution of electrons down to the energy levels available in quantum dots.

Due to the technological limitation of fabricating a device with a single quantum dot, I used a $2-$dimensional array of quantum dots as electron energy filter. However, it must be noted that the density of state function for single quantum dot $\rho_{QD}(E)$ is different from the density of state function for a 2-dimentional array of quantum dots $\rho_{2dQDs}(E)$. The density of state function $\rho_{2dQDs}(E)$ for 2-dimentional array of quantum dots is calculated by solving the electron wave-function in a potential consisting of quantum well $\delta - function$ modulated periodically in transverse direction. The calculation suggest that unlike individual quantum dots, 2-dimentional array of quantum dots result in a formation of miniband energy levels with band width of $\triangle E_{2dQDs} = 4\triangle$ and energy $\varepsilon_{1k} = E_0 + \triangle(2 - cosk_g b - cosk_z b)$(chapter 5). The bandwidth of minibands in 2-dimentional ar-

ray of quantum dots determine the "filtering capability" (or Q-factor) of quantum dots electron energy filters.

CdSe quantum dots are used for fabrication of energy filters. The device consist of $metal - insulator - 2dQDsArray - metal$ structure. Two different sets of devices are fabricated with device structure consisting of $ITO - Al_2O_3 - CdSeQDs - Ag$ and $Al - Al_2O_3 - CdSeQDs - Pb$ layers. The observation of negative differential resistance (NDR) in current-voltage measurement of $ITO - Al_2O_3 - CdSeQDs - Ag$ devices (figure 6.5) and stairs like characteristics for $Al - Al_2O_3 - CdSeQDs - Pb$ devices (figure 6.10) confirms that the electron transport is through minibands of 2-dimentional quantum dots array. The width $\triangle E_{2dQDs}$ of first miniband calculated using current-voltage measurement on $Al - Al_2O_3 - CdSeQDs - Pb$ device suggest that $\triangle E_{2dQDs} \sim 10mV$ (section 6.5). On the other hand, required energy filtering to resolve $HCOOH$ vibrational peak at room temperature is $\triangle E \sim 6.63mV$ (section 4.2). Hence, even though electron energy filtering is possible using quantum dots, its not enough to perform high resolution inelastic electron tunneling spectroscopy at room temperature.

Another important limitation of using quantum dots for energy filtering is "charge trapping". The observation of negative differential resistance (NDR) in current-voltage measurement of $ITO - Al_2O_3 - CdSeQDs - Ag$ devices and stairs like characteristics in $Al - Al_2O_3 - CdSeQDs - Pb$ devices gradually disappear with repeated scan of current-voltage measurement. The resistance of the device gradually increases with repeated IV measurement and eventually the device turn into off-state (i.e. very high impedance) (figure 6.12). This charge trapping in quantum dots is used as an advantage in quantum dot memory devices, however is a limitation for there application as electron energy filters.

8.2 Conclusion

Briefly, the conclusion of my thesis is as follows:

In order to perform inelastic electron tunneling spectroscopy at room temperature to resolve

vibrational energy level of molecules, thermal energy distribution of electrons should be less than $\triangle E \sim 6.63mV$. The designed quantum dots electron energy filters can only narrow down thermal distribution of electron down to only $\triangle E_{2dQDs} \sim 10mV$. Hence, even though quantum dot electron energy filters can narrow down thermal distribution of electrons from $\sim 25mV$ down to $\sim 10mV$, its not enough to perform high resolution inelastic electron tunneling spectroscopy at room temperature. Also, quantum dot energy filters suffer from charge trapping, which degrades there performance with repeated current-voltage measurement.

8.3 Discussion - Quantum dots vs Odorant Receptors

As we saw in chapter 5, unlike individual quantum dots, a 2-dimentional array of quantum dots result in a formation of energy minibands. The bandwidth of these minibands determines the "filtering capability" (or Q-factor) of quantum dots electron energy filters. This work suggest that, in order to improve the performance of electron energy filters, they should be fabricated using "single quantum dot" as compare to "array of quantum dots" used in this work.

If biological olfaction is based on IETS[1], doing IETS with odorant receptors proteins (figure 8.1) would involve addition and removal of electrons at well defined energy levels on either side of an odorant-sized binding site which serves as the tunneling gap. As shown in figure 8.1, the receptor protein accepts electrons from a soluble electron donor (NADPH). When the receptor binding site is empty , electrons are unable to tunnel across the binding site because no empty levels are available at the appropriate energy. When an odorant (here represented as an elastic dipole) occupies the binding site, electrons can lose energy during tunneling by exciting its vibrational mode. This only happens if the energy of the vibrational mode equals the energy gap between the filled and empty levels.

The study of electron transport through single quantum dots done in this work suggests that the size of the dot should be less than $\sim 2.5nm$ to be used in room temperature IET spectroscopy. Interestingly, this length scale is consistent with the size of donor and acceptor sites in odorant

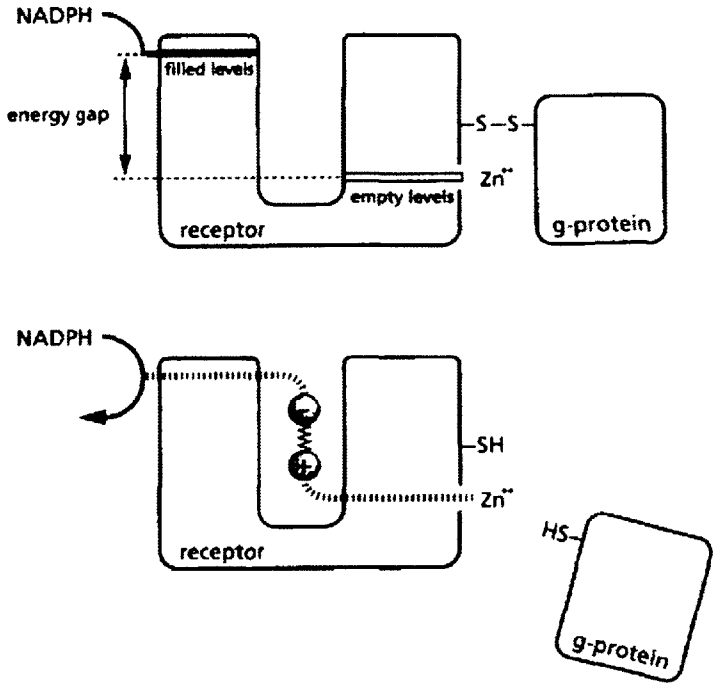

Figure 8.1: Schematic of the proposed IETS mechanism inside odorant receptors for molecular spectroscopy [1]

receptors potentially explaining how these receptors could be able to resolve molecular spectra at room temperatures.

8.4 Future Works

Based on the concussion of my thesis, following steps are suggested to further develop "electron energy filters"

1. To increase the Q-factor of electron energy filters, single quantum dots should be used.

2. This study used $480nm$ $CdSe$ quantum dots (size $\sim 2nm$). Further reducing the size of quantum dots is expected to increase the resolution with which electron energy filtering is possible.

3. Charge trapping at surface states of quantum dots depends upon the material property of

quantum dots. In order to avoid such charge trapping, another classes of quantum dots such as *PbS*, *PbSe* or graphene quantum dots can be studied.

Bibliography

[1] Turin, Chem. Senses, 1996, 21, 773

[2] Jaklevic and Lambe, J. Phys. ReV. Lett. 1966, 17, 1139

[3] P.K. Hansma 'Tunneling Spectroscopy', Plenum Press, New York (1982).

[4] K.W. Hipps and U. Mazur, J. Phys. Chem., 97, 7803

[5] K.W. Hipps, S.D. Williams and U. Mazur, Inorg. Chem., 23, 3500 (1984).

[6] Handbook of vibrational spectroscopy

[7] Keithley Nanotechnology Measurement Handbook 1st Edition

[8] Saumitra Raj Mehrotra; GerhardB Klimeck (2010), "Resonant Tunneling Diode operation," https://nanohub.org/resources/8799

[9] Narihiro M, Yusa G, Nakamura Y, Noda T and Sakaki H 1997, Appl. Phys. Lett. 70 105

[10] R. C. Jaklevic and J. Lambe, Phys. Rev. Lett. 17, 1139

[11] Yu B Lyanda-Geller and J-P Leburton, Semicond. Sci. Technol. 13 (1998) 35–42.

[12] J. C. C. Fan and J. B. Goodenough, Journal of Applied Physics, 48(8), 1977, pp. 3524 - 3531

[13] N. Balasubramanian and A. Subrahmanyam , Journal of Physics D: Applied Physics, 22, 1989, pp. 206 - 209

[14] J. Phys. Chem. B, Vol. 110, No. 10, 2006

[15] John C. C. Fan and John B. Goodenough, J. Appl. Phys. 48, 3524 (1977)

[16] H. E. Farnsworth and Ralph P. Winch, Phys. Rev. 58, 812–819 (1940)

[17] H. Mattoussi, L. H. Radzilowski, B. O. Dabbousi, E. L. Thomas, M. G. Bawendi, and M. F. Rubner, J. Appl. Phys. 83, 7965 1998

[18] Y. Gassenbauer and A. Klein , Solid State Ionics 173, 141–145

[19] M. D. Fischbein and M. Drndic, pplied physics letters 86, 193106

[20] Agilent 5500 AFM user manual

[21] Applied physics letters, vol 75 APPLIED PHYSICS LETTERS VOLUME 75, NUMBER 12 20 SEPTEMBER 1999

[22] Lucian Jdira1 et. al., physics review B 73, 115305 2006